Tryptophan metabolism reprogramming contributes to the prothrombotic milieu in mice and humans infected with SARS-CoV-2

Saravanan Subramaniam[1,2,*], Marc Arthur Napoleon[3,*], Saran Lotfollahzadeh[3], Mohamed Hassan Kamal[3], Helena Kurniawan[3], Murad Elsadawi[4], Devin Kenney[5,6], Florian Dhouam[5,6], Markus Bosmann[2,7], Stephen Whelan[8], Howard Cabral[9], Eric J Burks[4], Grace Zhao[4], Vijay Kolachalama[10], Katya Ravid[11], and Vipul C. Chitalia [#,3,4,12]

Authors affiliations:
[1]Department of Pharmacology and Toxicology, School of Pharmacy, Massachusetts College of Pharmacy and Health Sciences, Boston, MA 02115, USA
[2]Pulmonary Center, Department of Medicine, Chobanian & Avedisian School of Medicine, Boston University, Boston, MA 02118, USA
[3]Renal Section, Department of Medicine, Chobanian & Avedisian School of Medicine, Boston University, Boston, MA 02118, USA
[4]Department of Pathology and Laboratory Medicine, Chobanian & Avedisian School of Medicine, Boston University, Boston, MA 02118, USA
[5]Department of Virology, Immunology and Microbiology, Chobanian & Avedisian School of Medicine, Boston University, Boston, MA 02118, USA
[6]National Emerging Infectious Diseases Laboratories, Boston University, Boston, MA 02118, USA
[7]Center for Thrombosis and Hemostasis, University Medical Center of the Johannes Gutenberg-University, Mainz, Germany
[8]Chemical Instrumentation Center, Department of Chemistry, Boston University, Boston, MA, 02118, USA
[9]Department of Biostatistics, School of Public Health, Boston University, MA, 02118, USA
[10]Computational Medicine, Chobanian & Avedisian School of Medicine, Boston University, Boston, MA 02118, USA
[11]Department of Medicine and Whitaker Cardiovascular Institute, Chobanian & Avedisian School of Medicine, Boston University, Boston, MA 02118, USA
[12]Veterans Affairs Boston Healthcare System, Boston MA 02118, USA

**Shared first authors*

Manuscript type	Full article
Short Title	Kynurenine biogenesis and AHR-TF axis in COVID-19
Text	5005 words (max: 5,000-6,000 words)
Abstract	248 words (max: 250 words)
Main figures	8
Supplemental figures	4
Tables	2
References	55
Scientific category	Thrombosis and Hemostasis

#Corresponding author:
Vipul Chitalia, M.D., Ph.D.
Director, Center of Cross-Organ Vascular Pathology
Department of Medicine, Boston University Medical Center, X-545
Boston, MA 02118, USA

52 (P) 617-638-7330 (F) 617-638-7326
53 Email: vichital@bu.edu

54

Abstract

SARS-CoV-2 infection disturbs the coagulation balance in the blood, triggering thrombosis and contributing to organ failure. The role of prothrombotic metabolites in COVID-19-associated coagulopathy remains elusive. Leveraging K18-hACE2 mice infected with SARS-CoV-2, we observed higher levels of the tryptophan metabolite, kynurenine, compared to controls. SARS-CoV-2 infected mice showed a significant upregulation of enzymes controlling Kynurenine biogenesis, such as indoleamine 2,3-dioxygenase (IDO-1) and tryptophan 2,3-dioxygenase levels in kidneys and liver, respectively, as well as changes in the enzymes involved in kynurenine catabolism, including kynurenine monooxygenase and kynurinase. Consistent with the agonistic role of these metabolites in Aryl Hydrocarbon Receptor (AHR) signaling, AHR activation and its downstream mediator, tissue factor (TF), a highly potent procoagulant factor, was observed in endothelial cells (ECs) of lungs and kidneys of infected mice. These findings were validated in humans, where compared to controls, sera of COVID-19 patients showed increased levels of Kynurenine, kynurenic acid, anthranilic acid, and quinolinic acid. Activation of the AHR-TF axis was noted in the kidneys and lungs of COVID-19 patients, and COVID-19 sera showed higher IDO-1 activity than controls. Levels of Kyn in COVID-19 patients correlated strongly with the TF-inducing activity of COVID-19 sera on ECs. A specific IDO-1 inhibitor or AHR inhibitor separately or in combination suppressed COVID-19 sera-induced TF activity in ECs. Together, we identified IDO-1 as upregulated by SARS-CoV-2 infection, resulting in augmented Kyn and its prothrombotic catabolites, thereby suggesting the Kyn-AHR-TF axis as possibly a new diagnostic and/or therapeutic target.

Keywords: COVID-19, humanized ACE2 mice**,** tryptophan catabolism, kynurenine pathway

Key points:

1. SARS-CoV-2-infection upregulates kynurenine biogenesis in the liver and diminishes kynurenine catabolism in the lungs and kidneys.

2. An increase in kynurenine stimulates the AHR-TF axis in the microvasculature in COVID-19 patients, which is inhibited by pharmacological manipulation.

93 **Introduction**

94 SARS-CoV-2 infection induces a profoundly prothrombotic milieu by creating an imbalance
95 between pro- and anti-coagulant factors in the blood. This perturbation drives several thrombotic
96 complications in the arterial and venous beds of these patients, resulting in potentially fatal
97 complications such as pulmonary embolism, deep vein thrombosis, stroke, and coronary artery
98 syndrome [1-3]. In addition to macrovascular thrombosis, many studies demonstrated microthrombi
99 in the alveolar and renal capillary beds in mouse models [4,5] and humans [6,7]. Although thrombotic
100 complications are common in other viral infections, SARS-CoV-2 infection differentiates itself due
101 to a higher risk of thromboembolic phenomenon. COVID-19 results in approximately 9-fold higher
102 occurrence of alveolar microthrombi as compared to H1N1 patients [8 9,10]. Because microthrombi
103 are an important contributor to renal and respiratory failure, it is imperative to identify mediators
104 of microvascular thrombosis in these patients.

105 COVID-19-associated coagulopathy involves complex interactions between innate
106 immunity, extrinsic coagulation and fibrinolytic pathways, and the vascular endothelium, platelets,
107 and white blood cells (WBCs) [1,11,12]. Tissue factor (TF) is the primary trigger of the extrinsic
108 coagulation cascade during infection [1]. Blood from COVID-19 patients shows extrinsic
109 coagulation cascade activation, as evidenced by abnormal prothrombin time, and activated partial
110 thromboplastin time prolongation [2,13,14], supporting TF activation. TF is a membrane protein, and
111 its activation on the cell surface in different cell types, including endothelial cells (ECs), triggers
112 an extrinsic coagulation cascade [10,15].

113 A growing body of research points to the involvement of '*thrombolome*'—specific
114 metabolites with prothrombotic properties—in thrombosis in other disease models. Previous
115 studies from our lab and that of others showed that L-tryptophan (Trp)'s metabolites, such as L-
116 Kynurenine (Kyn) and its other catabolites, augment thrombosis in animal models and patients
117 with chronic kidney disease (CKD) [16-20] and in some cancer models [21]. A large portion of dietary
118 Trp (>80%) is converted in the liver to Kyn by a rate-limiting step catalyzed by tryptophan 2, 3-

119 dioxygenase (TDO) and indoleamine 2,3-dioxygenase (IDO). Kyn is further degraded by
120 Kynureninase or L-Kynurenine hydrolase (Kyn), Kynurenine aminotransferases (KATs) and 3-
121 hydroxyanthranilate oxidase (3-HAO) to different metabolites such as anthranilic acid (AA),
122 kynurenic acid (KYNA), xanthurenic acid (XA), quinolinic acid (QA) and picolinic acid (PA) to
123 generate nicotinamide adenine dinucleotide (NAD+) required for cellular metabolism [22] **(Figure**
124 **1A)**. The enzymes regulating Kyn biogenesis and degradation are expressed in different organs
125 and cell types. [23]. TDO is mainly expressed in the liver [24]. IDO expression is limited to dendritic
126 cells [25], vascular smooth muscle (vSMC) [26], and ECs [27].

127 Thomas et al. showed that the levels of Kyn were significantly higher in COVID-19 patients
128 [28], suggesting a potential alteration in Trp metabolism. Kyn is a ligand for aryl hydrocarbon
129 receptor (AHR). Kyn activates AHR signaling to upregulate TF in ECs and vSMC in other disease
130 models [18,21]. In the current study, we set out to examine the hypothesis that SARS-CoV-2 infection
131 upregulates enzymes controlling Kyn biogenesis and/or possibly suppresses enzymes involved
132 in Kyn catabolism in organs at risk of microvascular thrombosis. Leveraging genetically
133 humanized mice infected with SARS-CoV-2 and samples of infected humans (**Figure 1B)**, we
134 examined lungs, liver, and kidneys and employed pharmacological manipulations to probe the
135 targetability of the Kyn-AHR-TF axis.
136
137
138
139

140 **Methods**

141 **Mice**

142 Heterozygous transgenic humanized ACE2 (K18-hACE2) mice (strain: 2B6.Cg-Tg(K18-
143 ACE2)2Prlmn/J) were obtained from the Jackson Laboratory (Bar Harbor, ME). Animals were
144 maintained in Tecniplast green line individually ventilated cages (Tecniplast, Buguggiate, Italy).
145 Mice were maintained on a 12:12 light cycle at 30-70% humidity and provided *ad libitum* water
146 and standard chow diets (LabDiet, St. Louis, MO). The Boston University Biomedical Research
147 approved all experimental procedures with animals, Institutional Biosafety Committee and
148 Institutional Animal Care and Use Committee.

149 **SARS-CoV-2 propagation**

150 SARS-CoV-2 propagation was carried out following previously established methods[29,30]. The
151 SARS-CoV-2 isolate 2019-nCoV/USA-WA1/2020 (NCBI accession number: MN985325) was
152 sourced from the Centers for Disease Control and Prevention (Atlanta, GA) and BEI Resources
153 (Manassas, VA). $1x10^7$ African green monkey kidney Vero E6 cells (ATCC® CRL-1586™,
154 American Type Culture Collection, Manassas, VA) were seeded in a T-175 flask one day prior to
155 virus generation. The following day, the cells were infected with the virus diluted in 10 mL of Opti-
156 MEM (ThermoFisher Scientific, Waltham, MA, USA) and incubated for 1 hour at 37°C to facilitate
157 virus adsorption. Subsequently, 15 mL of DMEM containing 10% FBS and 1%
158 penicillin/streptomycin was added to the cells and incubated overnight. The next day, the media
159 was aspirated, cells were washed with 1X PBS, pH 7.5 (ThermoFisher Scientific), and 25 mL of
160 fresh DMEM containing 2% FBS was added. The cells were then monitored for cytopathic effect
161 (CPE), the media was harvested, filtered through a 0.22 µm filter, and concentrated using a
162 sucrose gradient. The concentrated virus was suspended in sterile 1X PBS, pH 7.5, aliquoted,
163 and stored at –80°C.

164 **SARS-CoV-2 titration via plaque assay**

165 The titer of our viral stocks was assessed using a plaque assay method. Vero E6 cells were plated
166 in a 12-well plate at a density of 2x10^5 cells per well. The following day, the cells were exposed
167 to 10-fold serial dilutions of the viral stocks and allowed to incubate for 1 hour at 37°C to enable
168 viral attachment. Subsequently, 1 mL of overlay media (composed of 1.2% Avicel (DuPont,
169 Wilmington, DE, USA; RC-581) in DMEM supplemented with 2% FBS and 1% Pen/Strep) was
170 added to each well. Three days later, the overlay media was removed, and the cells were fixed
171 with 10% neutral buffered formalin (ThermoFisher Scientific) for 1 hour at room temperature. After
172 fixation, the formalin was removed, and the cells were stained with 0.1% crystal violet (Sigma-
173 Aldrich) in 10% ethanol/water for 30 minutes at room temperature. Following staining, the crystal
174 violet was removed, cells were washed with water, and plaque-forming units were enumerated to
175 determine viral titers.

176 **SARS-CoV-2 inoculation of mice**

177 K18-hACE2 transgenic mice of both sexes (aged 12-16 weeks) were intranasally administered
178 with 1x10^6 plaque-forming units (PFU) of SARS-CoV-2 in 50 µL of sterile 1X PBS, or sham-
179 inoculated. The inoculations were conducted under 1-3% isoflurane anesthesia. Mice were
180 euthanized at predetermined time points for sample collection (2dpi, 4dpi, and 7dpi), or earlier if
181 they met euthanasia criteria (as defined by an IACUC-approved clinical scoring system).

182 **Cell culture**

183 Human umbilical vein endothelial cells (HUVEC)-TERT2 and HUVECs were cultured as described
184 before [18]. In brief, HUVEC-TERT2 cells were cultured in RPMI medium1640 (Cat. No. 11875-093,
185 GIBCO, MA), containing 10 % fetal bovine serum, 1% penicillin/streptomycin in 5% CO2 at 37°C.
186 HUVECs (Cat. no. C2517A; Lonza, Walkersville, MD) were cultured in EBM™-2 Basal Medium
187 (CC-3156) and EGMTM-2 SingleQuots™ Supplements (CC-4176) with 1% penicillin/streptomycin
188 in 5% CO2 at 37°C.

189

190

191 **COVID-19 sera and autopsy samples**

192 Sera samples and kidney autopsies from COVID-19 patients were received from Boston Medical
193 Center Biorepository (IRB: H26367 and IBC: 20-1459). Samples were collected from inpatient
194 and ambulatory patients who provided informed consent to participate in the study. Participants
195 were all confirmed positive for SARS-CoV-2 infection and were either admitted to the hospital or
196 seen in an ambulatory setting for treatment.

197 To this end, we recruited 29 patients at Boston Medical Center (BMC) with confirmed
198 COVID-19 of nasal epithelial PCR; most patients were male and had a mean age of 59 years.
199 These were mainly non-Hispanic white people who had a variety of comorbid conditions, such as
200 diabetes, hypertension, coronary artery disease, and stroke. Control patients admitted to BMC
201 over the same time were matched with members of this group. Most control patients were females
202 of black ethnicity and had comparable comorbidities; there were no statistical differences in age
203 between the control and COVID-19 groups (see Table 1).

204 **LC/MS-based metabolomics study**

205 Sera samples from COVID-19 patients and COVID-19-negative patients were used for LC/MS-
206 based metabolomics study as described before [31]. In brief, 200 μL of serum samples were
207 subjected to solid phase extraction using methanol and 1% formic acid. The analytes were eluted
208 with 1% ammonium peroxide in methanol/water (50:50). The elutes were dried under nitrogen
209 and reconstitute (150 μL) with 5 mmol/l ammonium acetate solution. For standards, ten
210 metabolites were weighed, dissolved in methanol, and diluted to specified concentrations in 5%
211 bovine serum albumin/phosphate-buffered saline (BSA/PBS) solution. Atlantis T3 C18 column
212 was used in HPLC (Waters, USA) for the separation of Trp metabolites with binary gradient
213 solvent consisting of solvent A mmol/l ammonium acetate) and solvent B (methanol). The flow
214 rate was 0.25 ml/min, and the injection volume was 10 μL. fractions were separated with positive
215 and negative mode. Mass spectrometry was equipped with an electrospray source. All seven
216 metabolites and their internal standards were infused into mass spectrometry for scanning the

217 spectrum and determining fragmentation. Selected parent/fragment pairs for each uremic solute
218 were used for mass spectrometry detection. Tryptophan, kynurenine, kynurenic acid, and
219 xanthurenic acid were detected in positive mode, while indoxyl sulfate, indoxyl acetate, and
220 anthranilic acid were detected in negative mode. The Institutional Review Board of Boston
221 University Medical Center, MA approved the protocol.

222 **Mouse tissue homogenization**

223 During necropsy, tissue samples were placed in 600 μL of RNA later (MilliporeSigma:
224 #R0901500ML) and preserved at −80°C. Prior to RNA extraction, 20–30 mg of tissue was
225 measured and transferred into a 2 mL tube containing 600 μL of RLT buffer with 1% β–
226 mercaptoethanol and a 5 mm stainless steel bead (Qiagen, Hilden, Germany: #69989). The tissue
227 was then dissociated using a Qiagen TissueLyser II (Qiagen) with the following cycle: two minutes
228 of dissociation at 1800 oscillations/min, one minute of rest, followed by another two minutes of
229 dissociation at 1800 oscillations/min. The dissociated tissues were centrifuged at 13,000 rpm for
230 10 minutes at room temperature, and the clear supernatant was carefully transferred to a new 1.5
231 mL Eppendorf tube before RNA extraction using TRIzol.

232 **Gene expression by RT-PCR**

233 Total RNA was extracted with TRIzol (Life Technologies, Carlsbad, CA) and transcribed into
234 cDNA using the QuantiTect Reverse transcription kit (Qiagen), and transcript levels were
235 quantified by TaqMan PCR assays with commercially available primer sets (Applied Biosystems),
236 by the $^{\Delta\Delta}$Ct method, with glyceraldehyde-3-phosphate dehydrogenase (GAPDH) as a normalizing
237 control [32].

238 **Cell surface TF activity**

239 As previously described, a two-step FXa generation assay was used to measure the TF
240 procoagulant activity in ECs [17,18,32]. In Brief, HUVECs were seeded in a 96-well plate (1000/well),
241 serum-starved for 16 h, then treated with 5% sera from COVID-19 patients for 24h with and
242 without AHR (CH223191; 10 μM) and IDO-1 (INCB024360; 10 μM) inhibitors. A standard plot

243 was generated by incubating human recombinant lipidated TF (Enzolifesciences, Cat# SE-537)
244 ranging from 0-500 pM along with 5 nM of human factor VIIa (Enzyme Research Laboratories
245 Cat# HF-VIIa) and 150 nM of factor X (Enzyme Research Laboratories Cat# HFX 1010) and
246 CaCl2- 5 mM for 30 min at 37 °C. A chromogenic substrate was added for factor Xa (Chromogenix
247 Cat# S2765, 1mM-final concentration) and then incubated for 5 min. The reaction was stopped
248 using 10 µL of 50% glacial acetic acid and read at 405 nm absorbance.

249 **AHR activity**

250 AHR activity was measured using HUVEC-TERT2 cells stably expressing a Cignal Lenti Reporter
251 xenobiotic response element tethered to luciferase reporter (XRE-luc) (Qiagen, CLS-9045L-8), as
252 previously described [21]. In brief, the cells were seeded at $1x10^3$ cells per well in 96-well plates.
253 Cells were starved for 16 hours and exposed to with and without AHR inhibitor CH223191
254 (Selleckchem, USA) in 5 % sera for 24 h. Firefly luciferase activity was measured using
255 PROMEGA's Dual Reporter Luciferase Assay Kit (cat#: E1980). The Luciferase signal (relative
256 luciferase activity unit) was normalized by total protein (Bradford protein assay kit; ThermoFisher,
257 MA, USA).

258 **IDO activity assay**

259 IDO activity was determined, as described previously,[33,34] and calculated by dividing the
260 detected concentration of Kyn in serum by that of Trp.

261

262 **Immunohistochemistry and immunofluorescence**

263 Following necropsy, mouse tissue samples were fixed for 72 hours in 10% neutral buffered
264 formalin. Tissues were then processed in a Tissue-Tek VIP-5 automated vacuum infiltration
265 processor (Sakura Finetek USA, Torrance, CA, USA), and subsequently, paraffin embedded
266 using a HistoCore Arcadia paraffin embedding station (Leica, Wetzlar, Germany).
267 Immunohistochemistry (IHC) and immunofluorescence (IF) were performed as previously
268 described [21]. In brief, paraffin embedded (liver, lungs, kidney, and aorta) tissue sections (5µm)

269 were deparaffinized and antigen retrieval was performed using 1X antigen unmasking solution
270 (Vector laboratories, H3300). For IHC, we used mouse and rabbit Specific HRP/DAB IHC
271 Detection Kit–Micro-polymer (ab236466) for the detection of specific antigens followed by tissues
272 counterstained with hematoxylin and eosin. The following antibodies used for IHC: Kynurenine 3-
273 monooxygenase (KMO) (Abcam, ab220922); Tryptophan 2,3-dioxygenase (TDO2) (Millipore,
274 MABN1537); Kynureninase (KYNU) (NOVUS, NBP1-56545); Indoleamine 2,3-dioxygenase (IDO-
275 1) (Millipore, MABF850). Dilution factors for these antibodies were provided in **supplemental**
276 **Table 1.**

277 For IF, tissues were permeabilized with 0.3% Triton X-100 in 1X phosphate-buffered saline
278 (PBS) for 10 min, blocked with 5% bovine serum albumin, and primary antibodies were probed
279 overnight at 4°C followed by secondary antibodies from Thermo Fisher Scientific (Alex Fluor 488,
280 594) for 45 min and counterstained with DAPI. The following antibodies used for IF: These
281 antibodies were CD31 (Abcam, ab28364); TF (Abcam, ab104513); AHR (Thermo Fisher
282 Scientific, MA1-514). Dilution factors for these antibodies were provided in **supplemental table**
283 **1.**

284 All images were obtained and quantified using the NikonQ17 Eclipse TE2000 Inverted
285 Microscope at the Boston University School of Medicine (BUSM) Imaging Core. For quantification,
286 the signal was converted to grayscale, and the number and intensity of pixels were analyzed as
287 integrated density by using Fiji software (version 2.9.0). The integrated density of all the images
288 was normalized to its area.

289 **Statistical analysis**

290 Statistical analysis was performed with Prism 8 software (GraphPad) by one-way analysis of
291 variance (ANOVA) for multiple groups and the Bonferroni multiple-comparisons test or
292 Student *t* test for 2 groups.

293

294 **Results**
295

296 *Alterations in the kynurenine pathway in liver, kidneys and lungs of humanized ACE2 mice*

297 Since TDO in the liver is the first enzyme in Kyn biogenesis, we examined the liver of K18-hACE2
298 mice infected with SARS-CoV-2 at 2dpi, 4dpi, 7dpi, and mock controls. The expression was
299 quantified using integrated density (ImageJ), which combines the intensity and pixel of signal and
300 normalizes to fixed area[21,35]. IHC of liver cross-sections **(Figure 2A[a-d])** and quantification **(Figure**
301 **2A[e])** showed that TDO levels increased at 2dpi (~3-fold) and peaked at 4dpi (~5-fold) and reverted
302 at 7dpi. Next, we examined other Kyn catabolic enzymes in **the** kidneys and lungs of K18-hACE2
303 mice infected with SARS-CoV-2. IHC of kidney cross-sections showed IDO-1 expression in the
304 renal tubules **(Figure 3A[a-d]**), and its expression increased ~3-fold in SARS-CoV-2-infected mice
305 at 2dpi and remained elevated until 7dpi compared to controls **(Figure 3A[e]**). Subsequently, we
306 tested downstream enzymes in Trp catabolism, such as Kynurenine-3-monooxygenase (KMO)
307 and L-kynureninase (KYNU). Interestingly, both KMO **(Figure 3B[a-d] and Figure 3B[e]**) and KYNU
308 **(Figure 3C[a-d] and Figure 3C[e]**) were downregulated in SARS-CoV-2 infected mice at 4dpi and
309 7dpi compared to control kidneys**.**

310 A similar analysis was performed in the lungs of K18-hACE2 mice infected with SARS-
311 CoV-2. IDO-1 expression in pulmonary epithelial cells was significantly upregulated at 2dpi (~ 2-
312 fold) and peaked at 4dpi (~4-fold) and reversed back at 7dpi compared to mock controls **(Figure**
313 **4A[a-d] and Figure 4A[e]**). KMO **(Figure 4B[a-d] and Figure 4B[e]**) and KNYU **(Figure 4C[a-d] and Figure**
314 **4C[e]**) expression significantly reduced in lungs at 2dpi, 4dpi and 7dpi compared to controls.

315 We further validated the expression of these enzymes using RT-PCR in liver, kidney, and
316 lungs. RT-PCR data revealed that TDO mRNA expression in liver was upregulated after SARS-
317 CoV-2 infection at 2dpi, 4dpi and significantly increased (~2-fold) at 7dpi compared to controls
318 **(supplemental Figure 1A)**. IDO-1 expression in lungs, but not in kidney, was significantly
319 upregulated at 2dpi and remained elevated at 4dpi and 7dpi compared to mock controls

320 **(supplemental Figures 1B-C)**. KMO and KYNU were downregulated in both kidney and lungs at
321 7dpi **(supplemental Figures 1D-G)**. As changes in the expression of IDO-1 protein in kidney did
322 not fully correspond to mRNA levels, these data suggest potential post-transcriptional regulation
323 of IDO-1 enzyme in this tissue. These findings suggest the upregulation of TDO1 in hepatocytes
324 and IDO-1 in kidney and lung ECs and the suppression of enzymes involved in KYN catabolism.
325

326 *Increase in Kynurenine biogenesis and activation of AHR signaling in SARS-CoV-2-infected mice*
327 Our data showed upregulation of KYN biogenesis enzyme and downregulation of enzymes
328 regulating KYN catabolism. This perturbation could result in an increase in KYN levels in the
329 blood. Thus, we examined mouse sera samples at 4dpi **(Figure 5A)** and sera from COVID-19
330 patients **(Figure 6A)**. Sera were analyzed using a pre-validated targeted metabolomics approach
331 using Liquid Chromatography Mass Spectrometry (LC-MS/MS) **(Figure 5A)** [18,36]. We observed a
332 significant increase in KYN (~3 to 4-fold; **Figure 5B**), KYNA (~6-fold; **Figure 5C**), and AA (~2-
333 fold; **Figure 5D**) in patients sera compared to non-infected controls. No significant changes in Trp
334 **(Figure 5E)** and QA **(Figure 5F)** were noted.

335 Since the above metabolites (???) are known AHR ligands, we examined this hypothesis
336 that AHR is activated in tissues of SARS-CoV-2-infected mice. Upregulation of nuclear AHR in
337 cells and their target genes, such as CYP1A1 and CYP1B1, are considered telltale signs of AHR
338 activation. Thus, we examined the mRNA expression of *Cyp1a1* and *Cyp1b1* by RT-PCR. *Cyp1b1*
339 was significantly upregulated in kidney lysates after 4dpi (~3-fold) and remained elevated at 7dpi
340 compared to mock controls **(supplemental Figure 2A).** Interestingly, we did see downregulation
341 of *Cyp1ba1 expression (*~2 to 4-fold*) at all-time points* **(supplemental Figure 2B)**.

342 *Cyp1b1* was also significantly upregulated (~2-fold) in lung lysates after 2dpi and remain
343 elevated at 4dpi and 7dpi compared to mock controls **(supplemental Figure 2B).** IF of kidney
344 vasculature and quantification revealed a reasonable increase in AHR (~2-fold) in ECs and sub-
345 ECs at 4dpi compared to mock controls **(Figure 5G-H)**. Similarly, AHR expression was

346 upregulated (~4-fold) in lung vasculature at 4dpi compared to mock controls **(supplemental**
347 **Figure 3A-B).**

348 TF is a potent activator of the coagulation pathway when it is expressed on the cell surface
349 [37]. We previously reported that the AHR-TF axis is associated with thrombosis after vascular injury
350 in humans[17] and in mouse cancer models subjected to venous thrombogenicity[21]. Thus, we
351 sought to investigate whether SARS-CoV-2 infection alters TF expression in the kidneys and
352 lungs of SARS-CoV-2-infected mice. RT-PCR revealed that TF mRNA expression was
353 upregulated in mice in both kidneys and lungs at all-time points **(supplemental figure 4A-B)**. IF
354 of kidney vasculature revealed a reasonable increase in TF (~4-fold) in ECs and sub-ECs at 4dpi
355 compared to mock controls **(Figure 5I-J)**. Similarly, IF of lung vasculature showed TF
356 upregulation (~2-fold) in lungs at 4dpi compared to mock controls **(supplemental Figure 3C-D).**
357 Overall, these findings suggested that increased expression of AHR and TF in the vasculature
358 could contribute to a prothrombotic milieu in the luminal region of K18-hACE2 mice infected with
359 SARS-CoV-2. This implied that the vascular beds were inflamed, which could regulate activation
360 of the extrinsic coagulation pathway via the AHR-TF axis.

361 *Kynurenine-AHR-TF axis in patients infected with SARS-CoV-2*

362 To enhance translational relevance, we assessed the above observations in 20 patients
363 confirmed to have SARS-CoV-2 infection between 2020-2022. Another group of patients negative
364 for COVID-19 admitted to the same hospital during the same period served as controls. **Table 1**
365 compares their baseline characteristics (see further details under methods).

366 COVID-19 patients had baseline heart rate, systolic blood pressure, and oxygen saturation
367 levels similar to those of control patients. Moreover, white blood cell counts, and platelet counts
368 were similar. Interestingly, ferritin was decreased in COVID-19-positive individuals, although the
369 data were incomplete. There was a considerable elevation of D-dimer in COVID-19-positive
370 patients, along with an increase in fibrinogen levels. About 40% of COVID-19 patients
371 experienced respiratory failure, 20% of patients died, and 27.5% of patients had renal failure. It is

important to highlight that patients' sera samples were taken at the time of admission, and their creatinine levels were normal. They had not experienced unusual symptoms up to that point.

Interestingly, by LC-MS/MS targeted proteomics, we observed a significant increase in Kyn (~2-fold; *p= .009*), kynurenic acid (~2-fold; *p= .003*), anthranilic acid (~1.5-fold; *p= .028*), and quinolinic acid (~0.5-fold; *p= .020*), in COVID-19 patients sera compared to controls **(Figure 6B-E)**. We did not find any change in tryptophan, xanthurenic acid, indoxyl sulfate and indoxyl acetate concentrations in sera of COVID-19 patients compared to controls **(Figure 6F-6I)**. Overall, these findings indicated systemic effect on Kyn catabolism that could potentially affect the luminal side of the vasculature, primarily ECs.

Elevated TF and AHR in ECs in Kidney autopsy from COVID-19 patients

We examined the kidney autopsies from five COVID-19 patients to validate the findings in clinical settings. Kidneys of the controls and COVID-19 autopsies were examined, and tissues were stained to detect AHR and TF. IF data revealed a basal expression of TF in controls and a significant increase in AHR (~ 3-fold; *p= .006*) **(Figure 6J-K)** and TF (~2-fold; *p= .002*) **Figure 6L-M)** expressions in kidney EC of COVID-19 autopsies compared to controls.

COVID-19 sera-mediated TF activation in human ECs can be suppressed by AHR or/and IDO-1 inhibitors.

Next, we posited that sera of COVID-19 patients with high Kyn levels can activate AHR signaling in EC, thereby upregulating TF-dependent prothrombotic activity. First, we examined AHR activity of pooled sera from COVID-19 patients in primary HUVECs. Sera samples from COVID-19 (n = 29) and control (n = 31) patients were combined respectively and added to cultured ECs that stably express the AHR response element coupled to luciferase reporter. Promega Dual Luciferase (PDL) assay (Promega, USA) was used to analyze the lysates after ECs were treated with 5% sera for 16 h **(Figure 7A)**. ECs exposed to COVID-19 sera exhibited significantly high AHR activity (~1.5-fold; *p= .043*) compared to control group sera **(Figure 7B)**. Similarly, there was a significant increase in surface procoagulant TF activity (~2-fold*; p= .0001*). IDO-1 activity in sera

398 was measured by the ratio of Kyn/Trp (see methods), which was ~1.5-fold; *p= .045* with COVID-
399 19 sera compared to control sera **(Figure 7C-D)**. TF activity induced in response to COVID-19
400 sera samples significantly correlated with AHR activity (*p= .045*) and IDO-1 activity (*p= .008*).
401 **(Figure 7E-F)**. Importantly, TF activity in ECs induced by sera of COVID-19 patients strongly
402 correlated with the Kyn levels (R^2 *= .562, P= .0001*) **(Figure 7G)**.

403 As a pharmacological approach, we used COVID-19 and control group sera (5%) with
404 increasing concentration of AHR inhibitor (CH223191) and examined AHR activity in ECs
405 expressing AHR luciferase reporter. There was a significant dose-dependent reduction in AHR
406 activity in both control and COVID-19 patients **(Figure 7H)**.

407 To further study the AHR-TF axis, we treated human primary ECs with COVID-19 or
408 control group sera (5%) with and without IDO-1 (INCB024360; 10μM) AHR (CH223191; 10μM)
409 inhibitors and measured TF activity. At baseline, COVID-19 sera alone induced a ~3-fold higher
410 TF activity in ECs compared to control sera **(Figure 7I)**. AHR inhibitor significantly reduced
411 endothelial TF activity upon both COVID-19 and control sera exposure **(Figure 7J)**. However, we
412 did not find notable changes in TF activity in ECs with IDO-1 inhibitor in the cell system **(Figure**
413 **8J).** It is possible that IDO-1 enzyme has no effect when a potent upstream regulator of TF, AHR
414 has a dominant influence. In accordance, a co-inhibition approach (both AHR and IDO-1
415 inhibitors) resulted in ~6-fold reduction in endothelial TF activity **(Figure 7J)** in injected samples
416 compared to controls.

417 Together, our results imply that cell-surface TF activity in ECs exposed to COVID-19 sera is
418 mediated by AHR ligands in the sera, which were synergistically inhibited by IDO-1 and AHR
419 inhibitors.

420

421 **Discussion**

422 Our data showed that SARS-CoV-2 infection in mice and humans upregulated Trp catabolism
423 due to differential regulation of key enzymes in Trp pathway in separate organs. Sera of patients
424 with COVID-19 showed higher levels of Kyn, and a specific set of downstream catabolites. These
425 results can be explained by the upregulation of TDO in liver, and IDO-1 enzyme in the lungs and
426 kidneys of SARS-CoV-2 infected mice, supporting an increase in Kyn biogenesis in systemic
427 (blood) and local milieu. This increase in Kyn levels is further accentuated by the downregulation
428 of KUNU and KMO in the lungs and kidneys, suppressing the catabolism of Kyn. Our work also
429 showed that sera samples from SARS-CoV-2-infected mice and humans activated AHR and TF
430 activity in the ECs, which were suppressed by combined inhibition of AHR and IDO-1 **(Figure 8)**.
431 Overall, this study demonstrates a previously unrecognized reprogramming of Trp metabolism
432 and activation of the AHR-TF axis in the ECs of lungs and kidneys in the context of SARS-CoV-
433 2. This data also suggests a combinatorial effect of AHR and IDO-1 inhibitors as candidate-
434 targeted antithrombotics in SARS-CoV-2 infected patients.

435 *Enzymes in Trp pathway in infections*

436 Trp and its metabolites regulate different biological processes, particularly in infection and
437 infection-related inflammation [38-42]. Enhanced Trp catabolism is associated with infection-induced
438 inflammation in *Chlamydia psittaci*, herpes simplex virus (HSV)-2, *Leishmania donovani*, and
439 *Toxoplasma gondii* [43]. However, these investigations did not compare the expression or regulation
440 of different enzymes in Trp metabolic pathway. Our work uncovers alterations in key rate-limiting
441 enzymes in Trp pathway such as IDO-1. *IDO-1* gene is regulated by interferon-α (IFNα), interferon
442 γ (IFNγ), TNF-α, and prostaglandins [44-47]. Recent work from our group showed that K18-hACE2
443 mice infected with SARS-CoV-2 had significant upregulation of plasma interferons (IFN-α/β/γ) and
444 cytokines (TNF-α and IL-6) levels at 2dpi and 4dpi [48], which is likely to explain upregulation of
445 *IDO-1* mRNA. Of note, KYNU and KMO expressions were downregulated without alterations in
446 their respective mRNAs, suggesting a potential post-transcriptional regulation of these enzymes.

447 Overall, our data suggest an interesting dichotomy in Kyn biogenesis and catabolizing enzymes
448 and their differential regulation in SARS-CoV-2 warranting further investigation.

449 Changes in the enzymes revealed an interesting pattern over the post-infection period and
450 may explain the chronology of thrombotic events in humans following SARS-CoV-2 infection. The
451 baseline expression of TDO in the liver was low and was induced for 2-4 days post-infection,
452 followed by suppression for seven days. In contrast, the expression of IDO-1 in renal tubules
453 remained persistently elevated for seven days post-infection. The baseline expression KMO and
454 KYNU was high in the kidneys and increased immediately post-infectious. However, their
455 expressions were suppressed from post-infectious day four onwards. These results suggest that
456 at baseline, Kyn metabolic homeostasis is biased towards its degradation. However, there is a
457 change in Kyn metabolism following SARS-CoV-2 infection. In the immediate period following
458 infection, enzymes in Kyn biogenesis and catabolism are increased simultaneously suggesting a
459 potential net neutral or mild increase in levels of Kyn. However, the elevation of Kyn levels is
460 sustained beyond four days post-infection by its increased biogenesis and reduced degradation.
461 The increase in the local levels of Kyn in specific organs is likely to trigger the downstream
462 signaling processes, such as the AHR-TF axis in the ECs of these organs, augmenting the risk of
463 thrombosis in specific organs following SARS-CoV-2. The analysis of Wuhan COVID-19 cases
464 showed systemic complications contributed by microvascular thrombosis, such as acute kidney
465 injury or respiratory failure in the second week of SARS-CoV-2 infection[49]. Cases from New York
466 also revealed events of arterial and venous thromboembolism between 8-14 days of initiation of
467 symptoms of COVID-19[50]. Overall, our data suggest a dynamic nature of Trp metabolism in
468 different organ systems, which may dictate the thrombotic risk in different organs.

469 *AHR-TF axis*

470 Our data advances the observations of other reports. A recent report demonstrated that
471 AHR is activated by SARS-CoV-2 infection to promote viral replication [51]. Another study of human
472 autopsies (66 patients with moderate to severe disease state) from COVID-19 patients

473 demonstrated that upregulation of pulmonary endothelial TF and downregulation of
474 thrombomodulin, a negative regulator of thrombosis, which correlated with elevated procoagulant
475 markers in blood [52]. Our results now show AHR as target of elevated Kyn in SARS-CoV-2
476 infection, with consequent upregulation of TF expression in ECs and induction of the extrinsic
477 coagulation cascade.

478 *Translational significance*

479 The translational relevance of our findings is underscored by the fact that prothrombotic
480 metabolites, such as Kyn, elicit potential targetable pathways such as AHR. Also, metabolite
481 generation can be pharmacologically manipulated. Both these approaches were explored to
482 manipulate TF activity assay on ECs. Because a AHR inhibitor suppressed TF activity more than
483 IDO-1 inhibitor, and both these inhibitors, when combined, had a higher TF suppressive effect, it
484 raises a possibility of AHR activation by ligands other than Kyn or its catabolites, i.e., independent
485 of IDO-1-mediated ligands. It is also possible that IDO1 inhibitor did not reduce Kyn to a threshold
486 level that is needed to avoid AHR activation. The notion of combinatorial antithrombotic stands to
487 reason, as prothrombotic propensity in COVID-19 patients requires a combination of therapies.
488 Also, targeting such pathways, which do not interfere with physiological hemostasis mechanisms,
489 is less likely to suffer from the major bleeding risk observed with Heparin[19,53]. These metabolites
490 can be explored further as a potential biomarker guiding therapy with IDO-1 and AHR inhibitors
491 as proposed in other human studies[34]

492 *Extended studies and conclusions*

493 This study employed pharmacological manipulation, which might affect several cell types in
494 context of whole-body physiology. Conditional knockout mice are required to establish a cell-type-
495 specific contribution of different enzymes to SARS-CoV-2-induced thrombosis. Secondly, our
496 study examined a set of Kyn degradation enzymes in two organs. Further investigation of other
497 organs and the entire enzyme machinery of tryptophan is needed to comprehensively understand
498 perturbations of Kyn metabolism. Similar to SARS-CoV-2, enveloped single-stranded RNA

499 viruses, such as Ebola, Marburg, Lassa, South American, yellow, Crimea-Congo, and Rift Valley,
500 cause prothrombotic complications[54]. Further studies are required to investigate the
501 generalizability of the role of tryptophan metabolites and the AHR-TF pathway in other infections.
502 SARS-CoV-2 has undergone several waves of mutations. It is important to compare the
503 alterations in Trp metabolism with mutant SARS-CoV-2 and wild-type SARS-CoV-2 as the
504 thrombotic risk is still observed with the mutant SARS-CoV-2[55].

505 In conclusion, SARS-CoV2's prothrombotic milieu can be explained by alterations in Trp
506 metabolism and activation of AHR-TF axis in ECs of specific organs. In doing so, we demonstrate
507 two anti-thrombotic pharmacological targets, AHR and IDO-1 in SARS-CoV-2, which supports
508 further in vivo studies and pre-clinical testing as additional therapies for coagulation abnormalities
509 in SARS-CoV-2 and possibly other viral related infections with thrombotic complications.

510

511

512

513

514 **Author contributions:** V.C conceptualized the overall study. V.C., K.R., and S.S. designed the
515 experimental study and offered conceptual insights. M.A.N., S.S., S.L., performed experiments
516 and immunofluorescence studies. F.D. and D.K. performed mouse infections and provided tissue
517 samples. M.H.K and H.K compiled COVID-19 patients' details. V.J., and M.E. quantified
518 immunohistochemistry slides. N.L. and S.W. performed a metabolomics study. G.Z., and E.B
519 performed autopsy studies. C.A., M.B., and J.F. contributed conceptually to experimental studies.
520 S.S., and V.C. interpreted data. S.S. wrote the manuscript. S.S., V.C., and K.R. reviewed and
521 revised the manuscript. All authors read and approved the manuscript.
522
523 **Acknowledgment:** We thank Prof Nigel Mackman (UNC Chapel Hill) for his assistance with the
524 TF activity assay.
525 **Funding support:** This work was funded in part by the Thrombosis and Hemostasis ARC and
526 the ARC on Respiratory Viruses: A Focus on COVID-19 (National Institutes of Health,
527 1UL1TR001430), DOM, BUSM, AHA Cardio-oncology SFRN CAT-HD Center grant 857078 (VCC
528 and SL), 1R01HL166608 (VCC and KR), and the Center for Cross Organ Vascular Pathology at
529 Boston University Department of Medicine (VCC). Mouse work was supported by a Boston
530 University Start-up fund (to F.D.). We thank the National Emerging Infectious Diseases
531 Laboratories (NEIDL) animal core for its outstanding support. We thank the Evans Center for
532 Interdisciplinary Biomedical Research at Boston University Chobanian & Avedisian School of
533 Medicine.
534
535
536
537
538
539

540

541

542

543

544 **Figure legends:**

545 **Figure 1: Schematic overview of Tryptophan catabolism**. **(A)** Diet with tryptophan is degraded
546 into two major segments. Ninety percent is absorbed and is converted to the N-Formylkynurenine
547 in the liver via two important enzymes, IDO-1/IDO-2 and TDO2. The remaining 10 % is converted
548 into indol. N-Formylkynurenine is converted to KYN via (Aryl) formamidase. However, N-
549 formylkynurenine is converted to kynurenic acid via (KAT-I/-II/-III). KYN is converted to 3-HK via
550 KMO. 3-HK is further degraded to XA, and to 3-HAA. The latter is catalyzed via Kynureninase
551 (KYNU). AA, anthranilic acid; ACMSD, aminocarboxymuconate-semialdehyde-decarboxylase;
552 AMO, anthranilate 3-monooxygenase; 3-HAA, 3-hydroxyanthranilic acid; 3-HAO, 3-
553 hydroxyanthranilate 3,4-dioxygenase; 3-HK, 3-hydroxykynurenine; IDO-1 and or, IDO-2,
554 indoleamine 2,3-dioxygenase-1 and -2; KATs, kynurenine aminotransferase enzymes; KMO,
555 kynurenine monooxygenase; KYN, kynurenine; KYNA, kynurenic acid; NAM, nicotinamide
556 adenine mononucleotide; PA, picolinic acid; QA, quinolinic acid; QPRT, quinolinate
557 phosphoribosyltransferase; TDO, tryptophan-2,3-dioxygenase; Trp, Tryptophan; XA, xanthurenic
558 acid. Enzymatic reactions are shown in *italics.* **(B) Schematic presentation of the experimental**
559 **design**. **(a)** Humanized transgenic ACE2 expressing mice were inoculated intranasally with
560 SARS-COV-2 and at specified time period, the mice were sacrificed, and organs (kidney, lung,
561 and liver) and blood samples were harvested. Samples were subjected to targeted tryptophan
562 metabolites. **(b)** Serum samples from COVID-19 patients were examined for **(i)** tryptophan
563 metabolites by LC-MS-based metabolomics and **(ii)** pooled serum (5%) exposure of human ECs,
564 followed by AHR and TF activity assays.

565

566 **Figure 2: TDO regulation in liver of humanized transgenic ACE2 mice infected with SARS-**
567 **CoV-2.** Mice were infected with SARS-CoV-2 and paraffin-embedded liver sections were made
568 at 2dpi, 4dpi, and 7dpi and screened for TDO-1 immunoreactivity (n=3 and imaged 3 different
569 locations per mouse). (a) Represents mice exposed to normal saline that serves as a mock

570 control; (b) 2dpi; (c) 4dpi, and (d) 7dpi. Scale bar = 100 micron; the inserts depict the zoomed-in
571 images. (e) Data were quantified and plotted as integrated density per micron. Data were
572 analyzed one-way ANOVA followed by multiple comparison test*. Significant ***P< .005.*
573
574 **Figure 3: IDO-1, KMO, and KYNU expression in renal tubules of** K18-hACE2 **mice infected**
575 **with SARS-CoV-2.** Mice were infected with SARS-CoV-2 and paraffin-embedded kidney sections
576 were made at 2dpi, 4dpi, and 7dpi and screened for (A) IDO-1, (B) KMO, and (C) KYNU
577 immunoreactivity (n=3 and imaged 3 different locations per mouse) in renal tubules. (a)
578 Represents the mice exposed to normal saline that serves as a mock control; (b) 2dpi; (c) 4dpi,
579 and (d) 7dpi in all three figures (A, B, and C). Scale bar = 100 micron; the inserts depict the
580 zoomed-in images. (e) Data were quantified and plotted as integrated density per micron of
581 respective markers (A, B, and C). Data were analyzed one-way ANOVA followed by multiple
582 comparison test. *Significant ***P< .005.*
583
584 **Figure 4: IDO-1, KMO, and KYNU expression in lungs of humanized transgenic ACE2 mice**
585 **infected with SARS-CoV-2.** Mice were infected with SARS-CoV-2 and paraffin-embedded lung
586 sections were made at 2dpi, 4dpi, and 7dpi and screened for (A) IDO-1, (B) KMO, and (C) KYNU
587 immunoreactivity (n=3 and imaged 3 different locations per mouse) in lungs. (a) Represents the
588 mice exposed to normal saline that serves as a mock control; (b) 2dpi; (c) 4dpi, and (d) 7dpi in all
589 three figures (A, B, and C). Scale bar = 100 micron; the inserts depict the zoomed-in images. (e)
590 Data were quantified and plotted as integrated density per micron of respective markers (A, B,
591 and C). Data were analyzed one-way ANOVA followed by multiple comparison test. *Significant*
592 ****P< .005*.
593
594 **Figure 5: LC/MS-based targeted metabolomics in sera and AHR and TF expression in renal**
595 **arteries from** K18-hACE2**mice (4dpi).** Sera samples from K18-hACE2mice infected with SARS-

596 CoV-2 were used for LC/MS-based metabolomic study (A). Separation was on Atlantis T3 C18
597 3μm 50 × 2.1 mm column Waters Corporation (MA, USA). A binary gradient consisting of solvent
598 A (5 mmol/l ammonium acetate) and solvent B (methanol) and different gradients were applied
599 (please see the method section for specific details about each metabolite). Mass spectrometry of
600 each metabolite was examined using API 4000 triple quadrupole mass spectrometry equipped
601 with electrospray and Agilent HPLC pump G1312B using plasma samples. All five metabolites
602 and their internal standards were infused into mass spectrometry for scanning spectrum and
603 determining fragmentation (B-F). All the metabolites were estimated from 4dpi sera and compared
604 to mock controls (n=5 per group). Metabolites: Tryptophan (Trp), kynurenine (KYN), kynurenic
605 mouse sera; *student t-test. *P < .05; n.s., not significant*. K18-hACE2 mice were infected with
606 SARS-CoV-2 and paraffin-embedded kidney sections were made at 4dpi and stained for (G) AHR
607 (I) TF. CD31 was used in both the panels (G and I) as an endothelial marker. Scale bar: panel A:
608 400X, Panel B: 200X). The yellow asterisk depicts the nuclear AHR expression, L: lumen. (H and
609 J) Data were quantified and plotted as integrated density per micron. Data were analyzed by
610 *student t-test*. *Significant *P< .05.*
611
612 **Figure 6: LC/MS-based targeted metabolomics in sera from COVID-19 patients and AHR**
613 **and TF expression in renal arteries from human autopsy.**
614 Sera samples from COVID-19 patients and healthy controls were used for LC/MS-based
615 metabolomic study (A). Separation was on Atlantis T3 C18 3μm 50 × 2.1 mm column Waters
616 Corporation (MA, USA). A binary gradient consisting of solvent A (5 mmol/l ammonium acetate)
617 and solvent B (methanol) and different gradients were applied (please see the method section for
618 specific details about each metabolite). Mass spectrometry of each metabolite was examined
619 using API 4000 triple quadrupole mass spectrometry equipped with electrospray and Agilent
620 HPLC pump G1312B using plasma samples. All seven metabolites and their internal standards
621 were infused into mass spectrometry for scanning spectrum and determining fragmentation (B-I).

622 All the metabolites were estimated from COVID-19 patients' sera and compared to matched
623 controls (n=20). Metabolites: Tryptophan (Trp), kynurenine (KYN), kynurenic acid (KYNA),
624 xanthurenic acid (XA), anthranilic acid (AA), quinolinic acid (QA), indoxyl sulfate (IS), indoxyl
625 acetate (IA); n = 20; each dot represent individual patients' sera; *student t-test*. *$P < .05$; **$P <$
626 $.01$; *n.s.,* not significant. Paraffin-embedded kidney sections were made from COVID-19-infected
627 human autopsy (64-YO) and stained for (J) AHR (L) TF. CD31 was used in both the panels (J
628 and L) as an endothelial marker. Scale bar = 100 microns. Inserts show a zoomed-in image of
629 the cells of interest. (K and M) Data were quantified and plotted as integrated density per micron
630 in ECs. L= lumen; White and blue arrowheads show the ECs. Data were analyzed by *student t-*
631 *test*. *Significant **P< .05; ***P< .005.*
632
633 **Figure 7: COVID-19 sera triggers AHR and TF activities in ECs. (A)** HUVEC-TERT2 were
634 exposed (16h) to COVID-19 patients' pooled sera (5%) were obtained from BU biorepositories
635 and measured AHR and TF activities. ECs that were genetically engineered stably expressing
636 AHR response aliment tethered to a luciferase reporter. Cells were subjected to 5% sera obtained
637 from control and patients with COVID-19. All the baseline characteristics of patients were shown
638 in supplemental table 1. Cells were exposed to sera for 16h and AHR activity was performed
639 using luciferase test. Data represent the individual samples with mean. *Significant **P< .01 by*
640 *student t- test.* **(B)** AHR activity in control and COVID-19 patients sera exposed ECs. **(C)** TF
641 activity in control and COVID-19 patients sera exposed ECs. **(D)** IDO-1 activity (sera levels of
642 KYN/Trp). **(E)** Spearman's rank correlation between TF activity and AHR activity. **(F)** Spearman's
643 rank correlation between TF activity and IDO-1 activity. **(G)** Spearman's rank correlation between
644 Kyn levels and TF activity. **(H)** AHR activity in control and COVID-19 patients subjected to the
645 different concentrations (1nM to 100μM) of AHR inhibitor (CH223191) and ECs were pre-treated
646 with control or COVID-19 sera along with AHR inhibitor (n=6). 2-way ANOVA for multiple groups
647 with time scale observations followed by Bonferroni post-hoc test; *Significant, *P < .05; n.s., not*

648 *significant*. Red circles represent WT; blue squares represent knock-out. **(I)** Pooled control and
649 COVID-19 sera samples (5%) were exposed to ECs for 16h with AHR inhibitor (CH223191; 0 to
650 20μM) and measured cell-surface TF activity. Data were analyzed two-way ANOVA followed by
651 multiple comparison test. *Significant ***P< .005*. Data were expressed as mean ± sem. n = 4;
652 *significant *P < .05*; **(J)** Pooled control and COVID-19 sera samples (5%) were exposed to ECs
653 for 16h with AHR inhibitor (CH223191; 10μM) and IDO-1 inhibitor (INCB024360; 10μM) and
654 measured TF activity. Data were expressed as mean ± sem. n = 6. Data were analyzed two-way
655 ANOVA followed by multiple comparison test. *Significant ns- non-significance, ***P< .001.*
656
657 **Figure 8: SARS-CoV-2-induced upregulation of IDO-1-Kyn-AHR axis induces a**
658 **prothrombotic vasculature.** Upregulated expression of IDO-1 in the vasculature of SARS-CoV-
659 2-infected mice or humans, and resulting elevation of serum Kyn, an AHR activator, result in
660 augmented levels of PAI-I and TF, the process of which is more effectively inhibited with both
661 IDO-1 and AHR inhibitors; *green color arrow and signs indicates activation of Kyn pathway during*
662 *SARS-CoV-2 infection in mice and human ECs; red color signs indicates inhibition of pathway by*
663 *small molecule inhibitor (IDO-1 and AHR inhibitors).*
664
665
666
667
668
669
670
671
672
673

674

675 **Supplemental figures**

676

677 **Supplemental Figure 1: Gene expression in liver, kidney, and lungs from** K18-hACE2**mice**
678 **infected with SARS-CoV-2**. K18-hACE2 mice were infected with SARS-CoV-2 and RNA was
679 isolated from liver, kidney, and lungs for gene expression by RT-PCR. (A) TDO2 expression in
680 liver (B) IDO-1 expression in kidney (C) IDO-1 expression in lungs (D) KMO expression in Kidney
681 (E) KMO expression in lungs (F) KYNU expression in kidney (G) KYNU expression in lungs. Data
682 were analyzed one-way ANOVA followed by multiple comparison test. Data were expressed as
683 mean ± SD; n=5-6 mice per group; *Significant: ns- non-significance, *P< .05, **P< .01.*

684

685 **Supplemental Figure 2: Cyp1b1 expression in kidney and lungs from** K18-hACE2 **mice**
686 **infected with SARS-CoV-2**. K18-hACE2 mice were infected with SARS-CoV-2 and RNA was
687 isolated from kidney and lungs for cyp1b1 expression by RT-PCR. (A) Cyp1b1 expression in
688 kidney (B) Cyp1b1 expression in lungs. Data were analyzed one-way ANOVA followed by multiple
689 comparison test. Data were expressed as mean ± SD; n=5-6 mice per group; *Significant: ns- non-*
690 *significance, *P< .05.*

691

692 **Supplemental Figure 3: AHR and TF expression in lung vasculature from** K18-hACE2 **mice**
693 **infected with SARS-CoV-2.** K18-hACE2 mice were infected with SARS-CoV-2 and paraffin-
694 embedded lung sections were made at 4dpi and stained for (A) AHR (C) TF. CD31 was used in
695 both the panels (A and C) as an endothelial marker. Scale bar = 100 microns. The yellow asterisk
696 depicts the nuclear AHR expression, L: lumen. (B and D) Data were quantified and plotted as
697 integrated density per micron. Data were analyzed by *student t-test. Significant **P< .01; ***P<*
698 *.001*.

699

700 **Supplemental Figure 4: TF expression in kidney and lungs from** K18-hACE2 **mice infected**
701 **with SARS-CoV-2**. K18-hACE2 mice were infected with SARS-CoV-2 and RNA was isolated from
702 kidney and lungs for TF expression by RT-PCR. (A) Cyp1b1 expression in kidney (B) Cyp1b1
703 expression in lungs. Data were analyzed one-way ANOVA followed by multiple comparison test.
704 Data were expressed as mean ± SD; n=5-6 mice per group; *Significant: ns- non-significance, *P<*
705 *.05.*
706
707
708
709
710
711
712
713
714
715
716
717
718
719
720
721
722
723
724
725

726 **Table 1. Baseline characteristics of patients**

	Control (N= 20)	COVID-19 (N= 20)	Significance (P value)
Age Mean (SD)	55.3±16.5	61.4±18.7	*0.281*
Sex number (%)			
Male	13 (65%)	15 (75%)	
Female	7 (35%)	5 (25%)	
Ethnicity			
Hispanic (%)	5	20	
Non-Hispanic (%)	45	30	
Race			
Caucasians (%)	17.5	20	
African Americans (%)	25	10	
Latino (%)	5	15	
Asian (%)	-	2.5	
Others# (%)	2.5	2.5	
Comorbidities			
HTN (%)	40 (8/20)	50 (10/20)	*0.525*
DM (%)	20 (4/20)	20 (4/20)	*1.00*
CAD (%)	20 (4/20)	5 (1/20)	*0.341*
CHF (%)	30 (6/20)	10 (2/20)	*0.235*
CKD (%)	100 (20/20)	100 (20/20)	*1.00*
Asthma (%)	25 (5/20)	20 (4/20)	*1.00*
COPD (%)	10 (2/20)	15 (3/20)	*1.00*
Cirrhosis (%)	0 (0/20)	10 (2/20)	*0.487*
Stroke (%)	15 (3/20)	15 (3/20)	*1.00*
Baseline vitals			
Pulse	94.4±21.7	88.8±12.1	*0.326*
SBP	135.9±22.3	130.4±21.9	*0.432*
DBP	78.8±15.3	77.8±8.7	*0.889*
SaO2	92.1±21.6	57.9±47.8	*0.007*
Temperature	98.7±1.3	98.6±1.1	*0.709*
Baseline labs			
Hb	10.8±3.2	12.1±2.8	*0.173*
WBC	9.7±5.7	8.4±3.9	*0.413*
Platelets	281.2±161.7	220.5±103.8	*0.165*
BUN (gm/dL)	16.7±9.8	17.1±9.9	*0.892*
Creatine (mg/dL)	1.0±0.4	0.98±0.43	*0.909*
Na (mEq/L)	138.3±2.5	137.6±4.9	*0.577*

K (mEq/L)	4.2±0.7	4.3±0.8	*.833*
CL (mEq/L)	105.4±4.3	104.5±5.1	*.531*
HCO3 (mEq/L)	22.3±3.9	22.5±3.5	*.866*
D-dimer	1810 ±617	4870.4 ±1057	.0182
Fibrinogen	382 ±218	412.9 ±103	.716

others- unknown race, mean (standard deviation), HTN- hypertension, DM- diabetes, COPD- chronic obstructive pulmonary disease, CKD excluded.

748 **Supplemental Table 1: Antibodies used for Immunohistochemistry and**

749 **immunofluorescence**

750

Antibody	Vendor	Catalog number	Dilution
kynurenine 3-monooxygenase	Abcam	(ab220922)	IHC- 1:50
Tissue Factor (TF)	Abcam	(ab104513)	IF- 1:100
CD31	Abcam	(ab28364)	IF- 1:50
IDO (Clone 1F8.2)	Millipore	MAB10009	IF- 1:10
IDO-1 (Clone 4B7)	Millipore	MABF850	IF- 1:10; IHC- 1:50
Kynureninase	Novus	NBP1-56545	IHC- 1:100
TDO2 (clone7A6.1)	Millipore	MABN1537	IHC- 1:50
AHR	Thermo Fisher Scientific	MA1-514	IF- 1:50

751

752

753

754

755

756

757

758

759

760

761

762

763 **References**

764 1. Subramaniam S, Kothari H, Bosmann M. Tissue factor in COVID-19-associated
765 coagulopathy. *Thromb Res*. 2022;220:35-47.

766 2. Kamel MH, Yin W, Zavaro C, Francis JM, Chitalia VC. Hyperthrombotic Milieu in COVID-19
767 Patients. *Cells*. 2020;9(11).

768 3. Mokhtari T, Hassani F, Ghaffari N, Ebrahimi B, Yarahmadi A, Hassanzadeh G. COVID-19
769 and multiorgan failure: A narrative review on potential mechanisms. *J Mol Histol*.
770 2020;51(6):613-628.

771 4. Vargas ESCF, Nguyen R, Willson M, et al. Intravital imaging of 3 different microvascular beds
772 in SARS-CoV-2-infected mice. *Blood Adv*. 2023.

773 5. Qin Z, Liu F, Blair R, et al. Endothelial cell infection and dysfunction, immune activation in
774 severe COVID-19. *Theranostics*. 2021;11(16):8076-8091.

775 6. Pellegrini D, Kawakami R, Guagliumi G, et al. Microthrombi as a Major Cause of Cardiac
776 Injury in COVID-19: A Pathologic Study. *Circulation*. 2021;143(10):1031-1042.

777 7. Parra-Medina R, Herrera S, Mejia J. Systematic Review of Microthrombi in COVID-19
778 Autopsies. *Acta Haematol*. 2021;144(5):476-483.

779 8. Khismatullin RR, Ponomareva AA, Nagaswami C, et al. Pathology of lung-specific thrombosis
780 and inflammation in COVID-19. *J Thromb Haemost*. 2021;19(12):3062-3072.

781 9. Ackermann M, Verleden SE, Kuehnel M, et al. Pulmonary Vascular Endothelialitis,
782 Thrombosis, and Angiogenesis in Covid-19. *N Engl J Med*. 2020;383(2):120-128.

783 10. Mackman N, Grover SP, Antoniak S. Tissue factor expression, extracellular vesicles, and
784 thrombosis after infection with the respiratory viruses influenza A virus and coronavirus. *J*
785 *Thromb Haemost*. 2021;19(11):2652-2658.

786 11. Subramaniam S, Ruf W, Bosmann M. Advocacy of targeting protease-activated receptors in
787 severe coronavirus disease 2019. *Br J Pharmacol*. 2022;179(10):2086-2099.

788 12. Conway EM, Mackman N, Warren RQ, et al. Understanding COVID-19-associated
789 coagulopathy. *Nat Rev Immunol*. 2022;22(10):639-649.

790 13. Lin J, Yan H, Chen H, et al. COVID-19 and coagulation dysfunction in adults: A systematic
791 review and meta-analysis. *J Med Virol*. 2021;93(2):934-944.

792 14. Wang L, He WB, Yu XM, Hu DL, Jiang H. Prolonged prothrombin time at admission predicts
793 poor clinical outcome in COVID-19 patients. *World J Clin Cases*. 2020;8(19):4370-4379.

794 15. Subramaniam S, Reinhardt C, Kulkarni PP, Spiezia L. Editorial: COVID-19 and thrombo-
795 inflammatory responses. *Frontiers in Cardiovascular Medicine*. 2023;10.

796 16. Chitalia VC, Shivanna S, Martorell J, et al. Uremic serum and solutes increase post-vascular
797 interventional thrombotic risk through altered stability of smooth muscle cell tissue factor.
798 *Circulation*. 2013;127(3):365-376.

799 17. Shivanna S, Kolandaivelu K, Shashar M, et al. The Aryl Hydrocarbon Receptor is a Critical
800 Regulator of Tissue Factor Stability and an Antithrombotic Target in Uremia. *J Am Soc*
801 *Nephrol*. 2016;27(1):189-201.

802 18. Kolachalama VB, Shashar M, Alousi F, et al. Uremic Solute-Aryl Hydrocarbon Receptor-
803 Tissue Factor Axis Associates with Thrombosis after Vascular Injury in Humans. *J Am Soc*
804 *Nephrol*. 2018;29(3):1063-1072.

805 19. Shashar M, Belghasem ME, Matsuura S, et al. Targeting STUB1-tissue factor axis
806 normalizes hyperthrombotic uremic phenotype without increasing bleeding risk. *Sci Transl*
807 *Med*. 2017;9(417):1-11.

808 20. Shashar M, Francis J, Chitalia V. Thrombosis in the uremic milieu--emerging role of
809 "thrombolome". *Semin Dial*. 2015;28(2):198-205.

810 21. Belghasem M, Roth D, Richards S, et al. Metabolites in a mouse cancer model enhance
811 venous thrombogenicity through the aryl hydrocarbon receptor-tissue factor axis. *Blood*.
812 2019;134(26):2399-2413.

813 22. Savitz J. The kynurenine pathway: a finger in every pie. *Mol Psychiatry*. 2020;25(1):131-147.

814 23. Murakami Y, Saito K. Species and cell types difference in tryptophan metabolism. *Int J*
815 *Tryptophan Res*. 2013;6(Suppl 1):47-54.

816 24. Capece L, Arrar M, Roitberg AE, Yeh SR, Marti MA, Estrin DA. Substrate stereo-specificity in
817 tryptophan dioxygenase and indoleamine 2,3-dioxygenase. *Proteins*. 2010;78(14):2961-
818 2972.

819 25. Dai X, Zhu BT. Indoleamine 2,3-dioxygenase tissue distribution and cellular localization in
820 mice: implications for its biological functions. *J Histochem Cytochem*. 2010;58(1):17-28.

821 26. Cuffy MC, Silverio AM, Qin L, et al. Induction of indoleamine 2,3-dioxygenase in vascular
822 smooth muscle cells by interferon-gamma contributes to medial immunoprivilege. *J Immunol*.
823 2007;179(8):5246-5254.

824 27. Beutelspacher SC, Tan PH, McClure MO, Larkin DF, Lechler RI, George AJ. Expression of
825 indoleamine 2,3-dioxygenase (IDO) by endothelial cells: implications for the control of
826 alloresponses. *Am J Transplant*. 2006;6(6):1320-1330.

827 28. Thomas T, Stefanoni D, Reisz JA, et al. COVID-19 infection alters kynurenine and fatty acid
828 metabolism, correlating with IL-6 levels and renal status. *JCI Insight*. 2020;5(14).

829 29. Carossino M, Kenney D, O'Connell AK, et al. Fatal Neurodissemination and SARS-CoV-2
830 Tropism in K18-hACE2 Mice Is Only Partially Dependent on hACE2 Expression. *Viruses*.
831 2022;14(3).

832 30. Kenney DJ, O'Connell AK, Turcinovic J, et al. Humanized mice reveal a macrophage-
833 enriched gene signature defining human lung tissue protection during SARS-CoV-2 infection.
834 *Cell Rep*. 2022;39(3):110714.

835 31. Zhang A, Rijal K, Ng SK, Ravid K, Chitalia V. A mass spectrometric method for quantification
836 of tryptophan-derived uremic solutes in human serum. *J Biol Methods*. 2017;4(3).

837 32. Subramaniam S, Ogoti Y, Hernandez I, et al. A thrombin-PAR1/2 feedback loop amplifies
838 thromboinflammatory endothelial responses to the viral RNA analogue poly(I:C). *Blood Adv*.
839 2021;5(13):2760-2774.

840 33. Suzuki Y, Suda T, Asada K, et al. Serum indoleamine 2,3-dioxygenase activity predicts
841 prognosis of pulmonary tuberculosis. *Clin Vaccine Immunol*. 2012;19(3):436-442.

842 34. Walker JA, Richards S, Whelan SA, et al. Indoleamine 2,3-dioxygenase-1, a Novel
843 Therapeutic Target for Post-Vascular Injury Thrombosis in CKD. *J Am Soc Nephrol*.
844 2021;32(11):2834-2850.

845 35. Arinze NV, Yin W, Lotfollahzadeh S, et al. Tryptophan metabolites suppress Wnt pathway
846 and promote adverse limb events in CKD patients. *J Clin Invest*. 2021.

847 36. Zhang A, Rijal K, Ng SK, Ravid K, Chitalia V. A mass spectrometric method for quantification
848 of tryptophan-derived uremic solutes in human serum. *J Biol Methods*. 2017;4(3):1-8.

849 37. Mackman N. Role of tissue factor in hemostasis, thrombosis, and vascular development.
850 *Arterioscler Thromb Vasc Biol*. 2004;24(6):1015-1022.

851 38. Mehraj V, Routy JP. Tryptophan Catabolism in Chronic Viral Infections: Handling Uninvited
852 Guests. *Int J Tryptophan Res*. 2015;8:41-48.

853 39. Kavoussi L, Mikkelson D, Clayman R. Re: Rectal perforation as a complication of urethral
854 instrumentation: 2 case reports. *J Urol*. 1989;142(5):1333-1334.

855 40. Ye Z, Yue L, Shi J, Shao M, Wu T. Role of IDO and TDO in Cancers and Related Diseases
856 and the Therapeutic Implications. *J Cancer*. 2019;10(12):2771-2782.

857 41. Pantouris G, Mowat CG. Antitumour agents as inhibitors of tryptophan 2,3-dioxygenase.
858 *Biochem Biophys Res Commun*. 2014;443(1):28-31.

859 42. Curti A, Trabanelli S, Salvestrini V, Baccarani M, Lemoli RM. The role of indoleamine 2,3-
860 dioxygenase in the induction of immune tolerance: focus on hematology. *Blood*.
861 2009;113(11):2394-2401.

862 43. Schmidt SV, Schultze JL. New Insights into IDO Biology in Bacterial and Viral Infections.
863 *Front Immunol*. 2014;5:384.

864 44. Werner ER, Bitterlich G, Fuchs D, et al. Human macrophages degrade tryptophan upon
865 induction by interferon-gamma. *Life Sci*. 1987;41(3):273-280.

866 45. von Bergwelt-Baildon MS, Popov A, Saric T, et al. CD25 and indoleamine 2,3-dioxygenase
867 are up-regulated by prostaglandin E2 and expressed by tumor-associated dendritic cells in
868 vivo: additional mechanisms of T-cell inhibition. *Blood*. 2006;108(1):228-237.

869 46. Carlin JM, Borden EC, Sondel PM, Byrne GI. Interferon-induced indoleamine 2,3-
870 dioxygenase activity in human mononuclear phagocytes. *J Leukoc Biol*. 1989;45(1):29-34.

871 47. Popov A, Abdullah Z, Wickenhauser C, et al. Indoleamine 2,3-dioxygenase-expressing
872 dendritic cells form suppurative granulomas following Listeria monocytogenes infection. *J*
873 *Clin Invest*. 2006;116(12):3160-3170.

874 48. Subramaniam S, Hekman RM, Jayaraman A, et al. Platelet proteome analysis reveals an
875 early hyperactive phenotype in SARS-CoV-2-infected humanized ACE2 mice. *bioRxiv*.
876 2021:2021.2008.2019.457020.

877 49. Zhou F, Yu T, Du R, et al. Clinical course and risk factors for mortality of adult inpatients with
878 COVID-19 in Wuhan, China: a retrospective cohort study. *Lancet*. 2020;395(10229):1054-
879 1062.

880 50. Griffin DO, Jensen A, Khan M, et al. Arterial thromboembolic complications in COVID-19 in
881 low risk patients despite prophylaxis. *Br J Haematol*. 2020.

882 51. Giovannoni F, Li Z, Remes-Lenicov F, et al. AHR signaling is induced by infection with
883 coronaviruses. *Nat Commun*. 2021;12(1):5148.

884 52. Francischetti IMB, Toomer K, Zhang Y, et al. Upregulation of pulmonary tissue factor, loss of
885 thrombomodulin and immunothrombosis in SARS-CoV-2 infection. *EClinicalMedicine*.
886 2021;39:101069.

887 53. Paranjpe I, Fuster V, Lala A, et al. Association of Treatment Dose Anticoagulation With In-
888 Hospital Survival Among Hospitalized Patients With COVID-19. *J Am Coll Cardiol*.
889 2020;76(1):122-124.

890 54. Iba T, Levy JH, Levi M. Viral-Induced Inflammatory Coagulation Disorders: Preparing for
891 Another Epidemic. *Thromb Haemost*. 2022;122(1):8-19.

892 55. Oba S, Hosoya T, Amamiya M, et al. Arterial and Venous Thrombosis Complicated in
893 COVID-19: A Retrospective Single Center Analysis in Japan. *Front Cardiovasc Med*.
894 2021;8:767074.
895

Figure 1

A

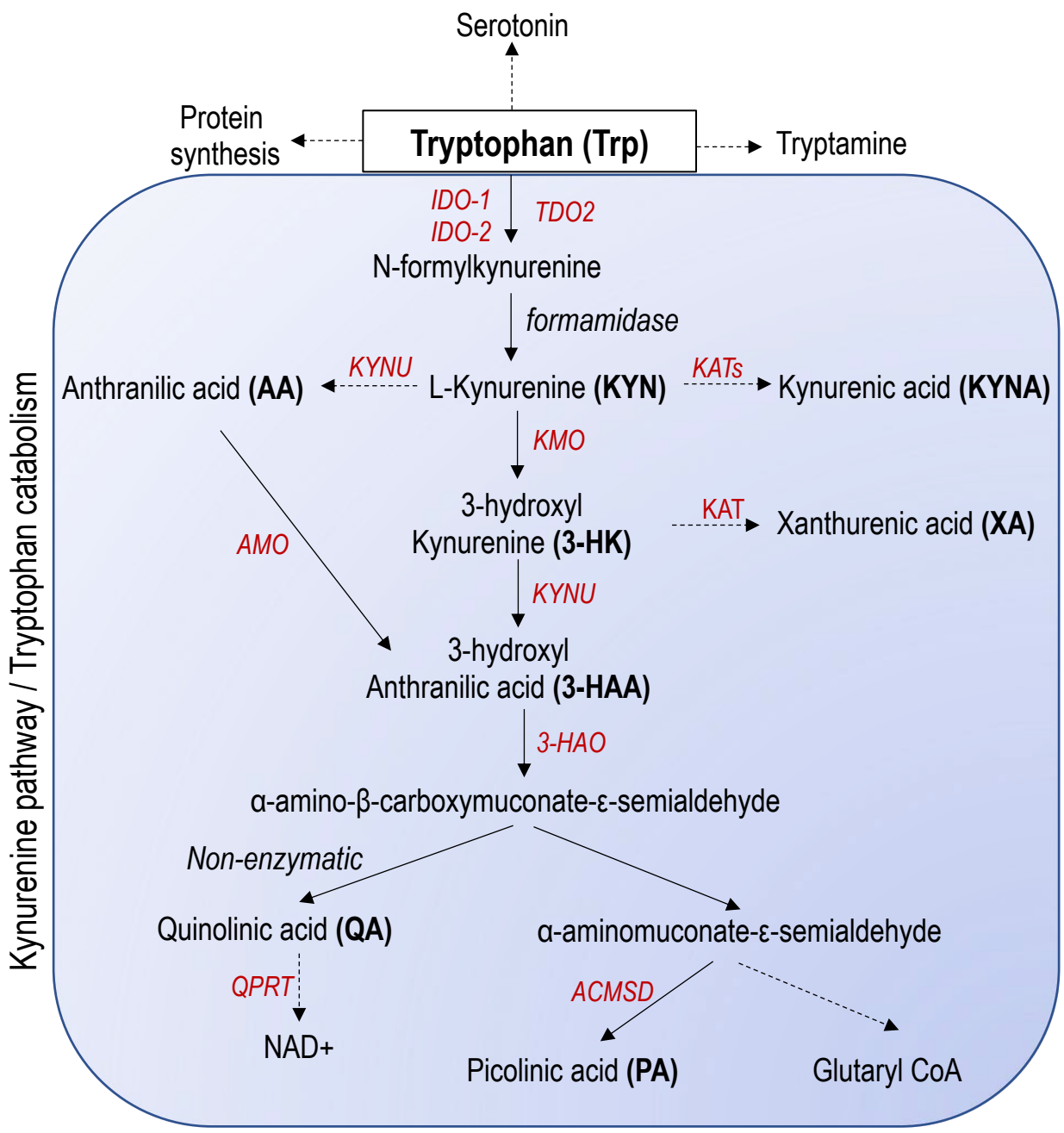
Serotonin
Protein synthesis
Tryptophan (Trp)
Tryptamine
IDO-1
IDO-2
TDO2
N-formylkynurenine
formamidase
KYNU
KATs
Anthranilic acid (AA)
L-Kynurenine (KYN)
Kynurenic acid (KYNA)
KMO
3-hydroxyl Kynurenine (3-HK)
KAT
Xanthurenic acid (XA)
AMO
KYNU
3-hydroxyl Anthranilic acid (3-HAA)
3-HAO
α-amino-β-carboxymuconate-ε-semialdehyde
Non-enzymatic
Quinolinic acid (QA)
α-aminomuconate-ε-semialdehyde
QPRT
ACMSD
NAD+
Picolinic acid (PA)
Glutaryl CoA
Kynurenine pathway / Tryptophan catabolism

B

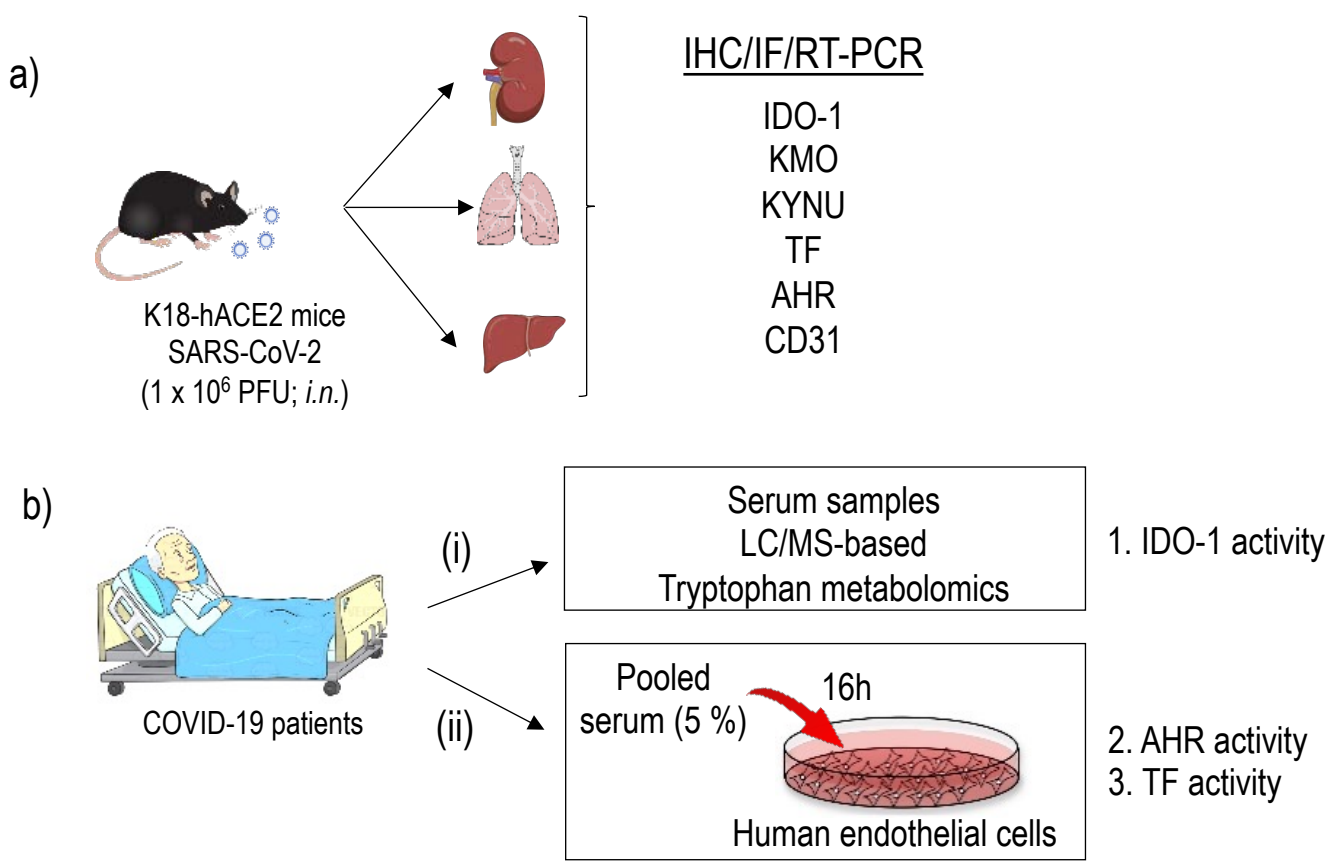
a)
K18-hACE2 mice
SARS-CoV-2
(1 x 10^6 PFU; i.n.)
IHC/IF/RT-PCR
IDO-1
KMO
KYNU
TF
AHR
CD31
b)
COVID-19 patients
(i)
(ii)
Serum samples
LC/MS-based
Tryptophan metabolomics
1. IDO-1 activity
Pooled serum (5 %)
16h
Human endothelial cells
2. AHR activity
3. TF activity

Figure 2

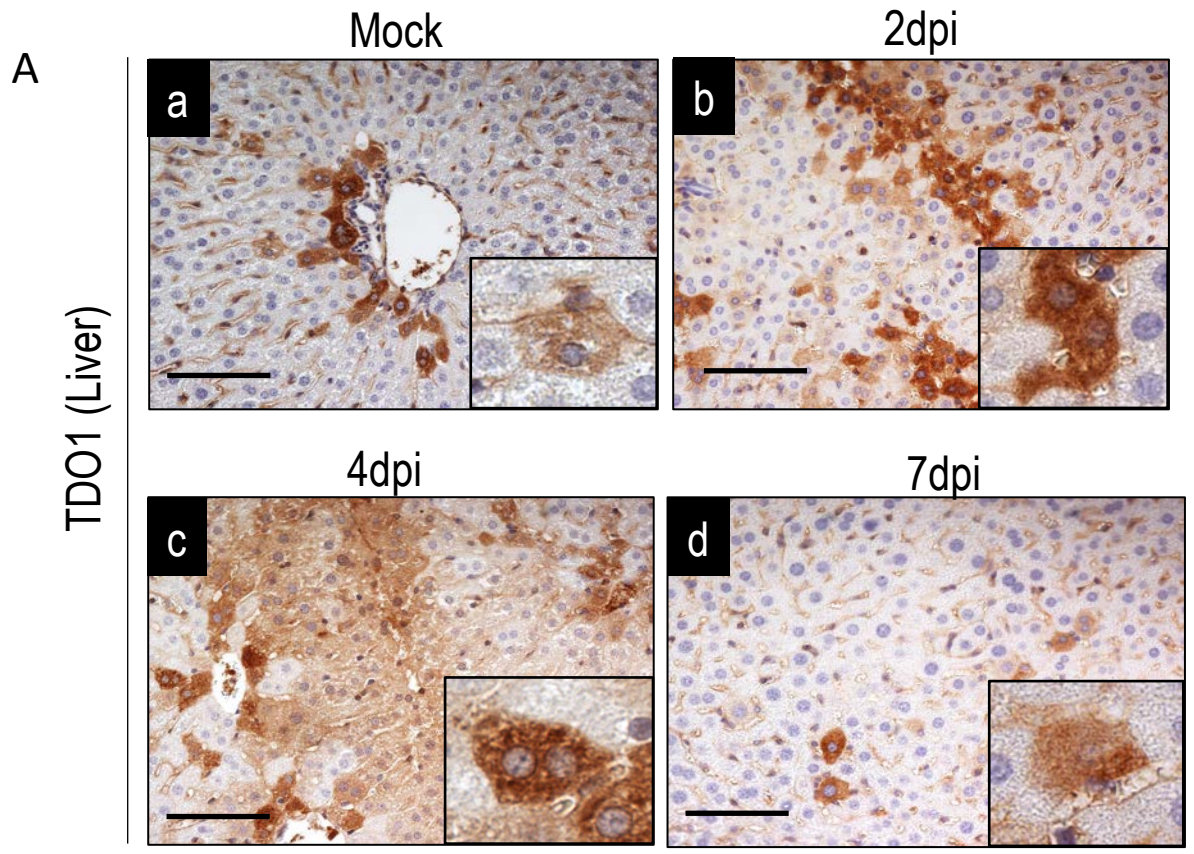
A
TDO1 (Liver)
Mock
2dpi
4dpi
7dpi
a
b
c
d

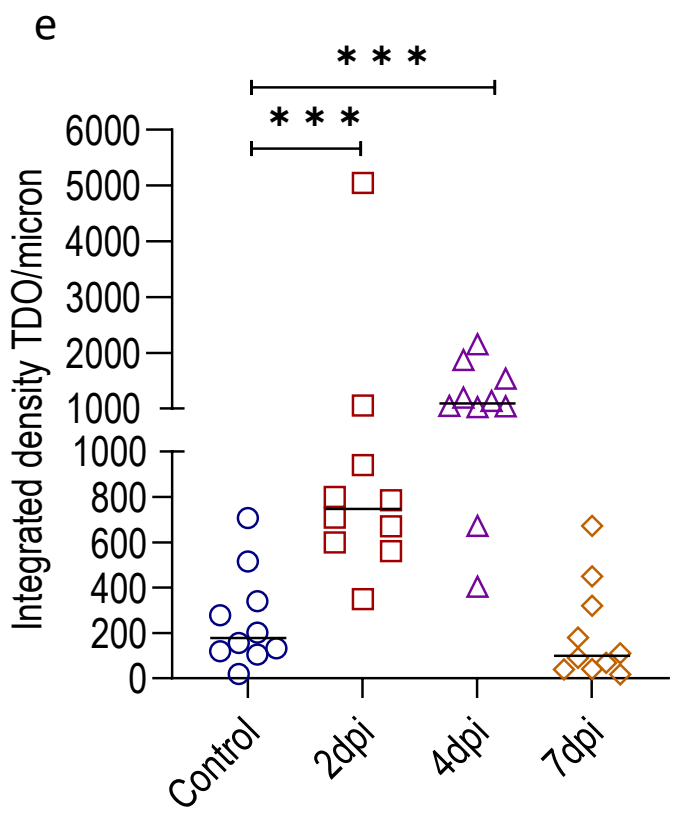
e
Integrated density TDO/micron
6000
5000
4000
3000
2000
1000
1000
800
600
400
200
0
* * *
* * *
Control
2dpi
4dpi
7dpi

Figure 3

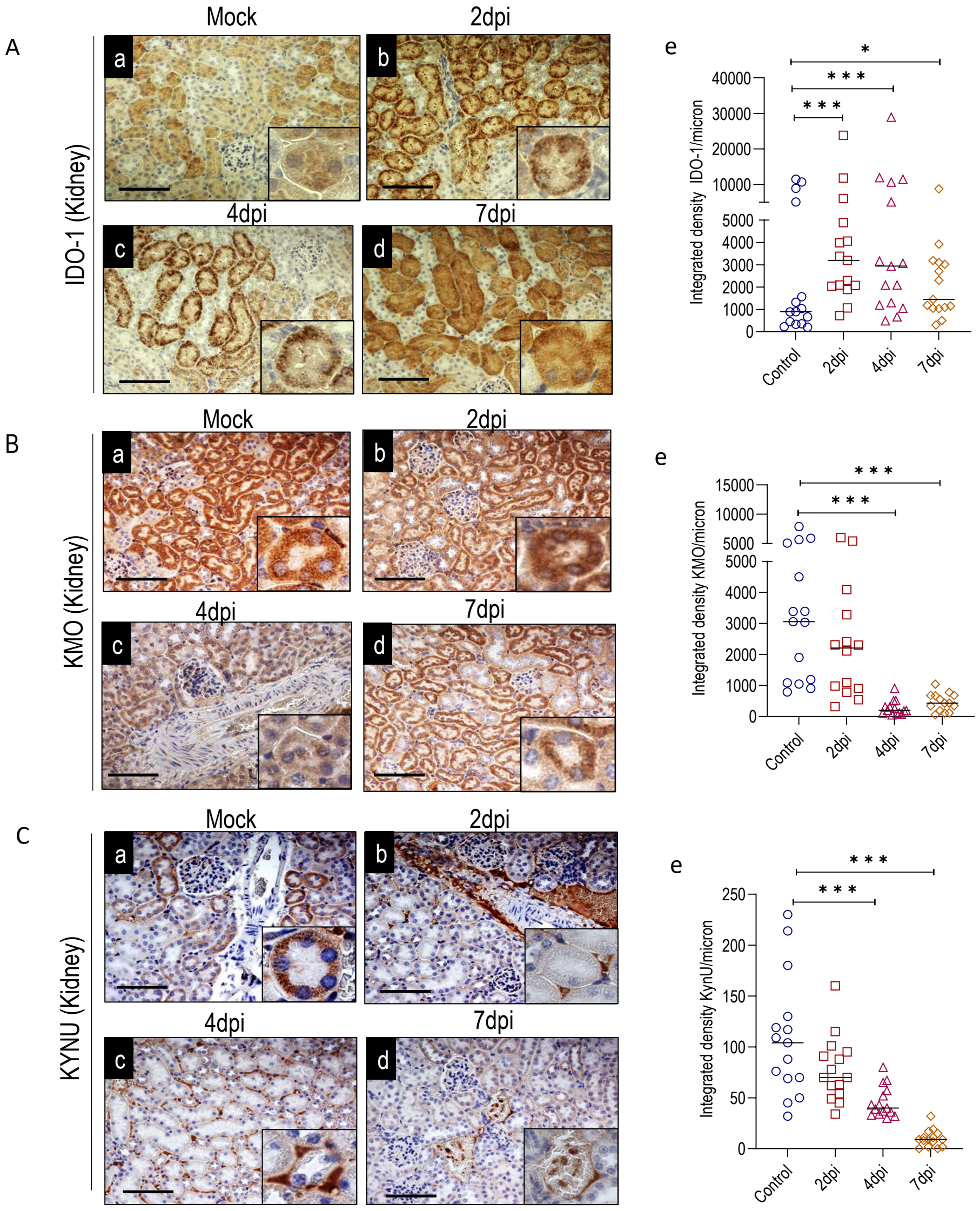
A
IDO-1 (Kidney)
Mock
2dpi
4dpi
7dpi
a
b
c
d
e
Integrated density IDO-1/micron
40000
30000
20000
10000
5000
4000
3000
2000
1000
0
Control
2dpi
4dpi
7dpi
B
KMO (Kidney)
Mock
2dpi
4dpi
7dpi
a
b
c
d
e
Integrated density KMO/micron
15000
10000
5000
5000
4000
3000
2000
1000
0
Control
2dpi
4dpi
7dpi
C
KYNU (Kidney)
Mock
2dpi
4dpi
7dpi
a
b
c
d
e
Integrated density KynU/micron
250
200
150
100
50
0
Control
2dpi
4dpi
7dpi

Figure 4

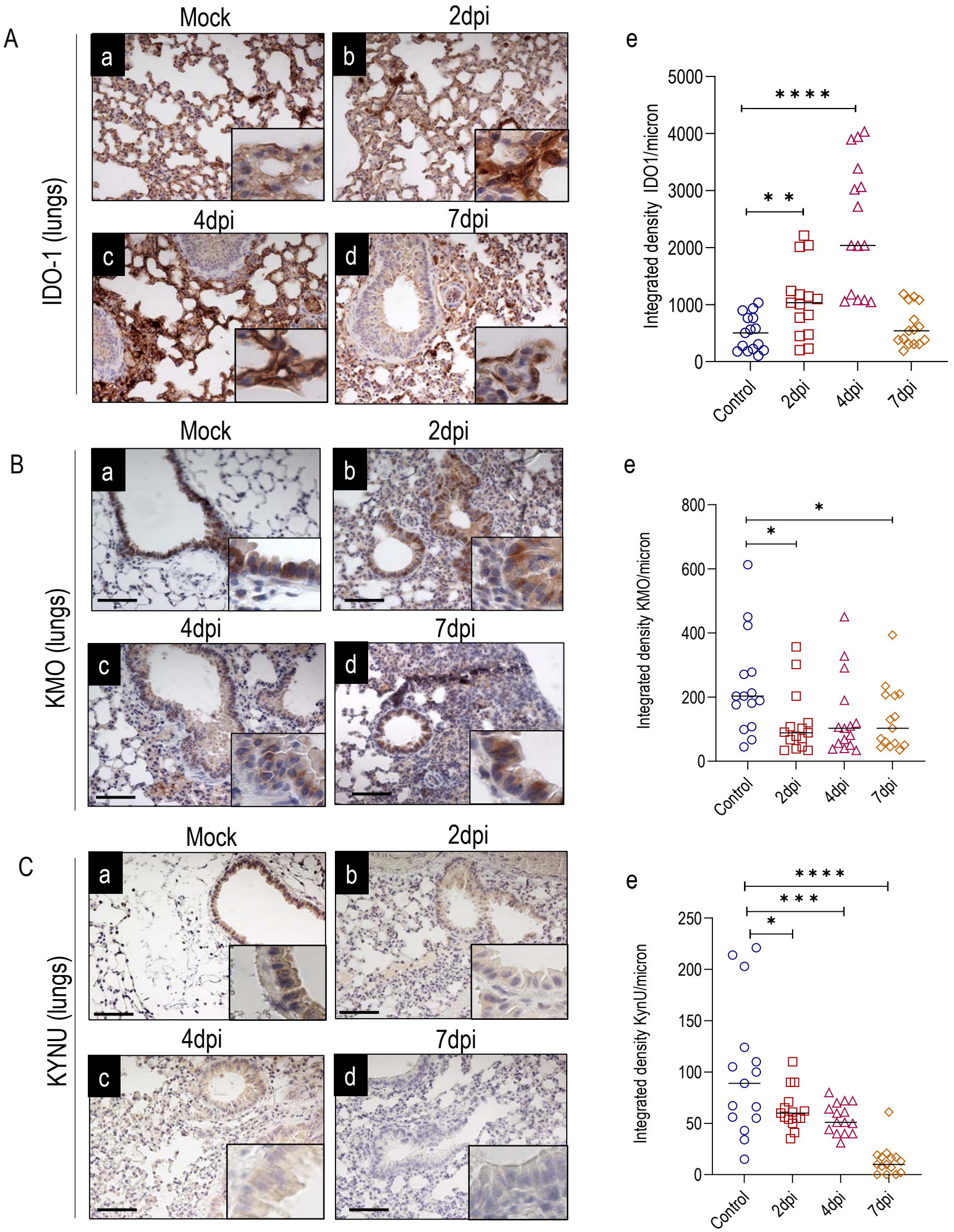
A
IDO-1 (lungs)
Mock
2dpi
4dpi
7dpi
a
b
c
d
e
Integrated density IDO1/micron
5000
4000
3000
2000
1000
0
* * * *
* *
Control
2dpi
4dpi
7dpi
B
KMO (lungs)
Mock
2dpi
4dpi
7dpi
a
b
c
d
e
Integrated density KMO/micron
800
600
400
200
0
*
*
Control
2dpi
4dpi
7dpi
C
KYNU (lungs)
Mock
2dpi
4dpi
7dpi
a
b
c
d
e
Integrated density KynU/micron
250
200
150
100
50
0
* * * *
* * *
*
Control
2dpi
4dpi
7dpi

Figure 5

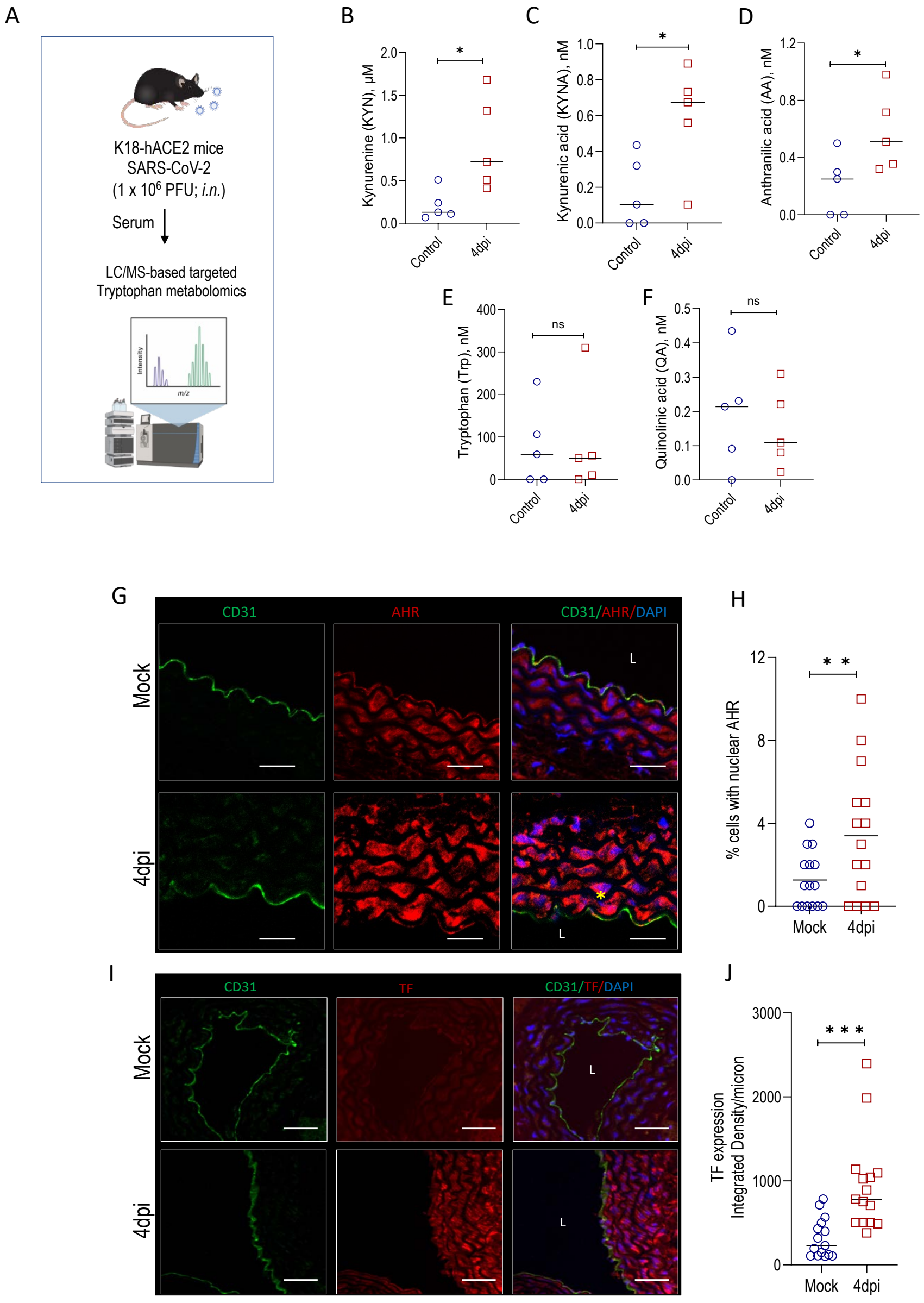
A
K18-hACE2 mice
SARS-CoV-2
(1 x 10^6 PFU; i.n.)
Serum
LC/MS-based targeted
Tryptophan metabolomics
Intensity
m/z
B
Kynurenine (KYN), µM
Control
4dpi
C
Kynurenic acid (KYNA), nM
D
Anthranilic acid (AA), nM
E
Tryptophan (Trp), nM
ns
F
Quinolinic acid (QA), nM
G
CD31
AHR
CD31/AHR/DAPI
Mock
4dpi
L
H
% cells with nuclear AHR
Mock
I
TF
CD31/TF/DAPI
J
TF expression
Integrated Density/micron

Figure 6

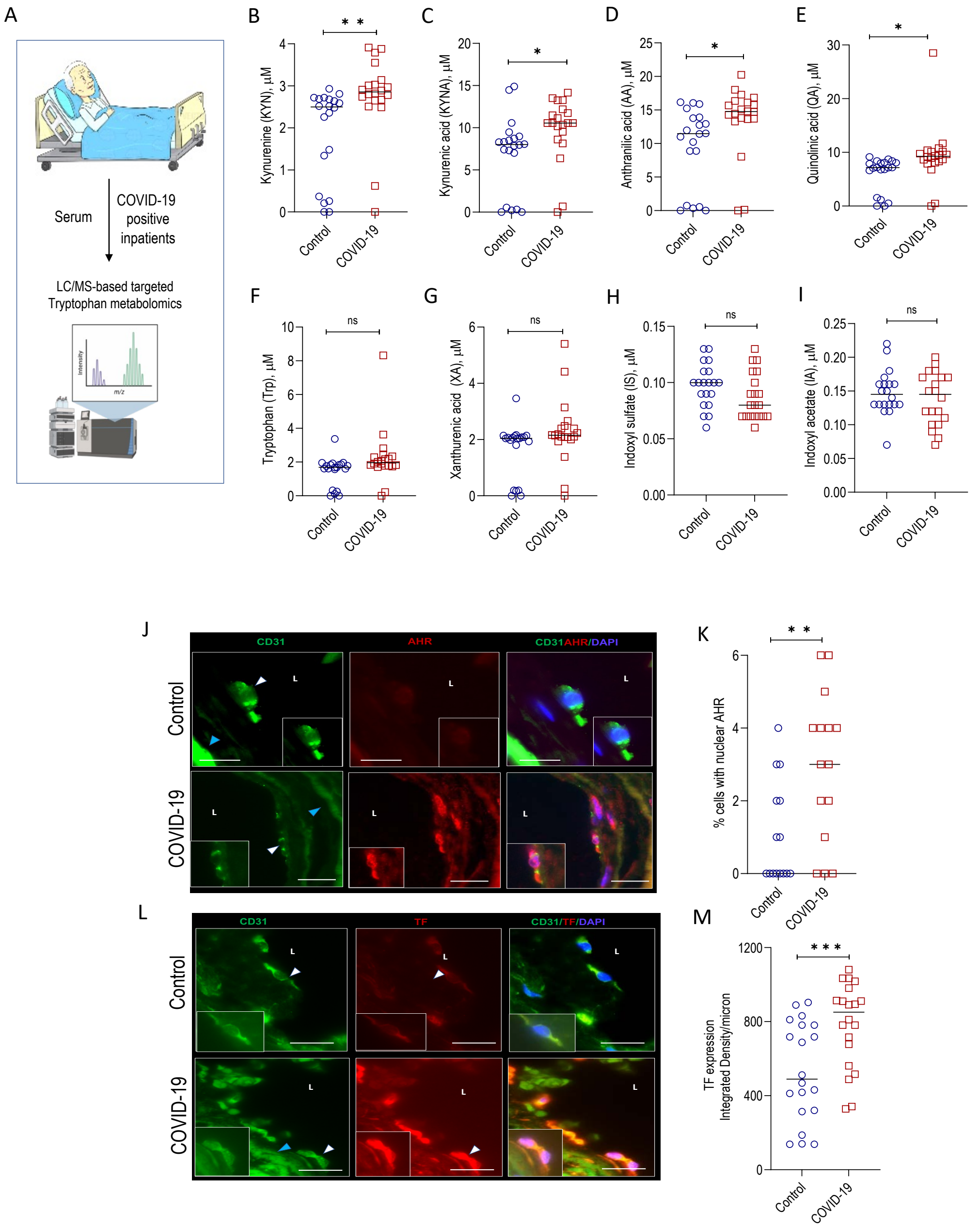
A
Serum
COVID-19 positive inpatients
LC/MS-based targeted Tryptophan metabolomics
Intensity
m/z
B
Kynurenine (KYN), µM
Control
COVID-19
C
Kynurenic acid (KYNA), µM
D
Anthranilic acid (AA), µM
E
Quinolinic acid (QA), µM
F
Tryptophan (Trp), µM
ns
G
Xanthurenic acid (XA), µM
H
Indoxyl sulfate (IS), µM
I
Indoxyl acetate (IA), µM
J
CD31
AHR
CD31AHR/DAPI
Control
COVID-19
K
% cells with nuclear AHR
L
CD31
TF
CD31/TF/DAPI
M
TF expression Integrated Density/micron

Figure 7

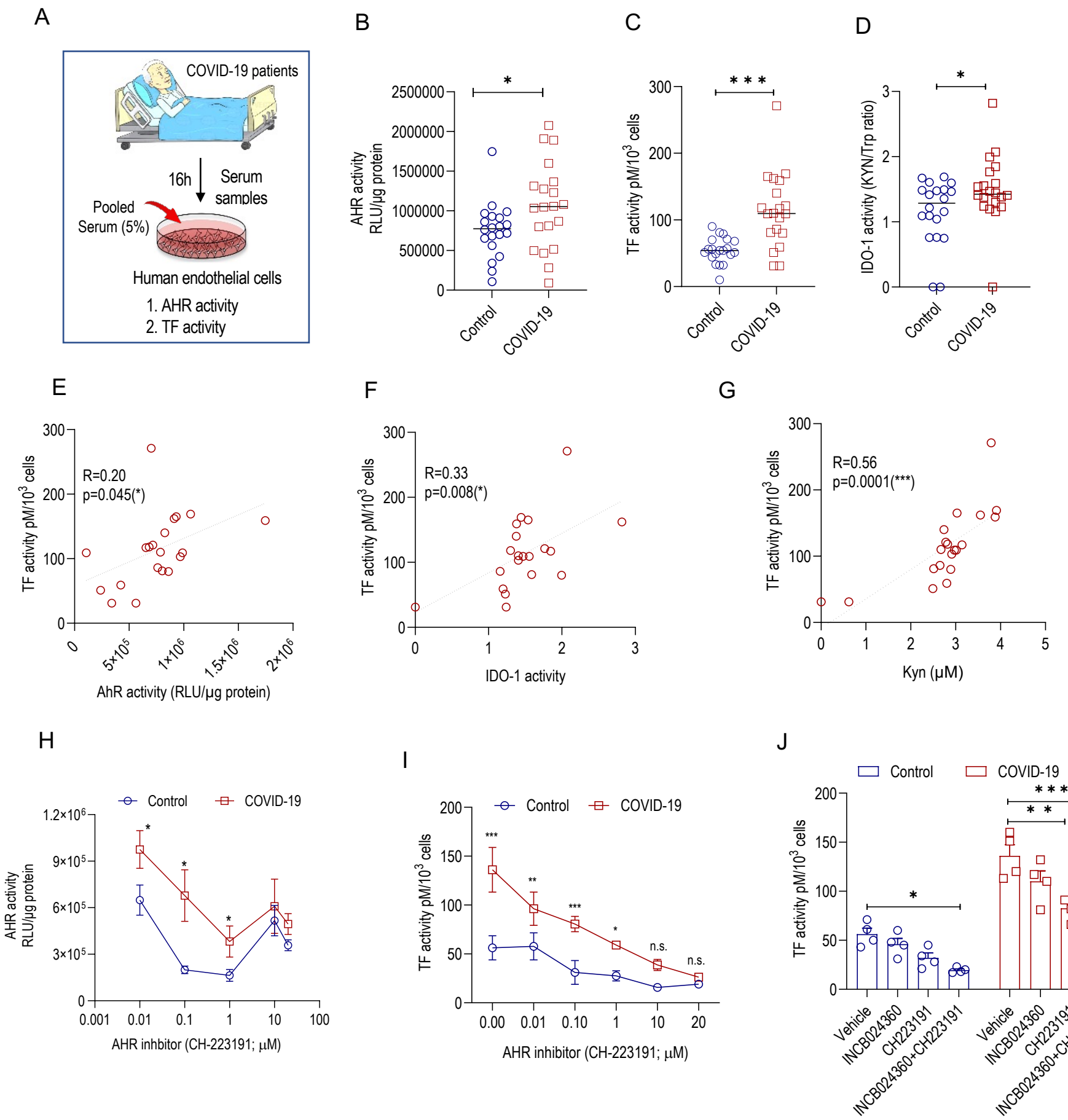
A
COVID-19 patients
16h
Serum samples
Pooled Serum (5%)
Human endothelial cells
1. AHR activity
2. TF activity
B
AHR activity RLU/µg protein
Control
COVID-19
C
TF activity pM/10^3 cells
D
IDO-1 activity (KYN/Trp ratio)
E
R=0.20
p=0.045(*)
AhR activity (RLU/µg protein)
F
R=0.33
p=0.008(*)
IDO-1 activity
G
R=0.56
p=0.0001(***)
Kyn (µM)
H
AHR inhbitor (CH-223191; µM)
I
AHR inhibitor (CH-223191; µM)
n.s.
J
Vehicle
INCB024360
CH223191
INCB024360+CH223191

Figure 8

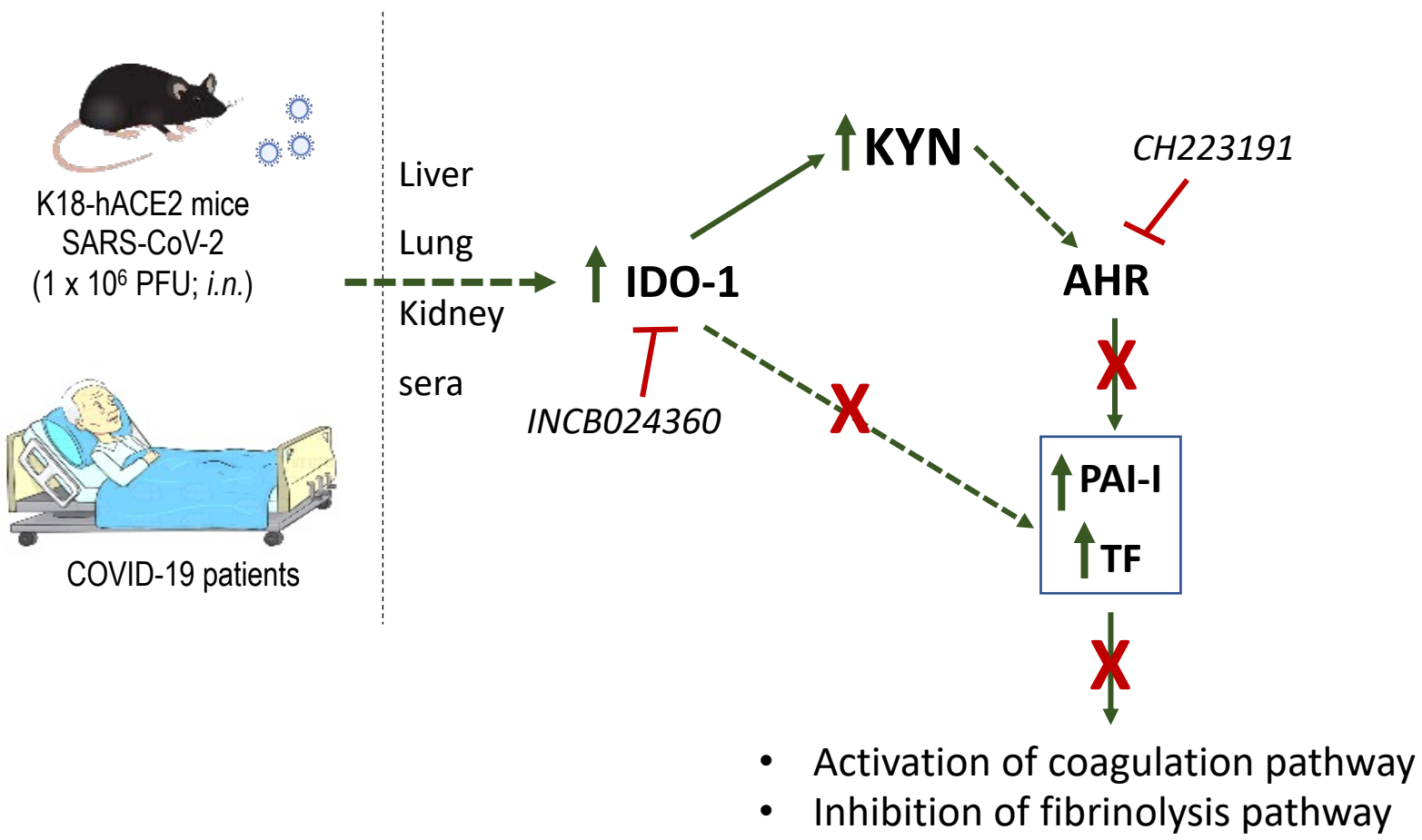
K18-hACE2 mice
SARS-CoV-2
(1 x 10⁶ PFU; i.n.)
COVID-19 patients
Liver
Lung
Kidney
sera
IDO-1
KYN
AHR
CH223191
INCB024360
PAI-I
TF
Activation of coagulation pathway
Inhibition of fibrinolysis pathway

Supplemental Figures

Supplemental Figure 1

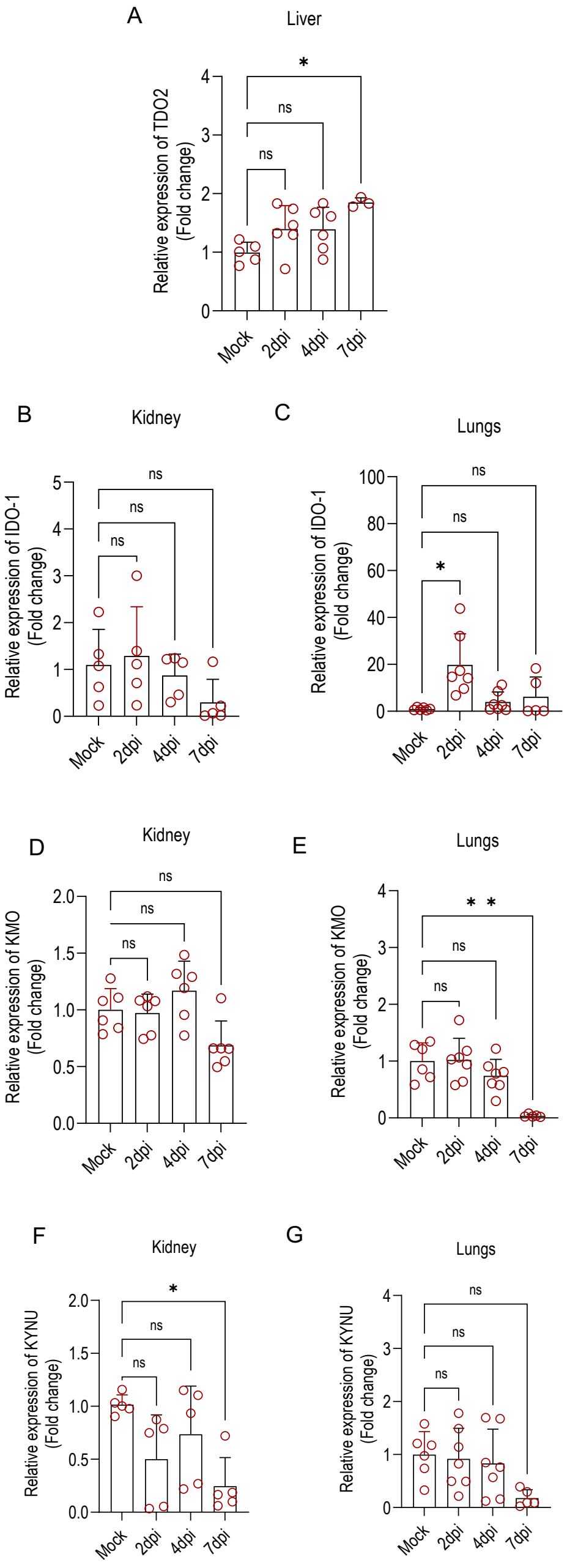

Supplemental Figure 2

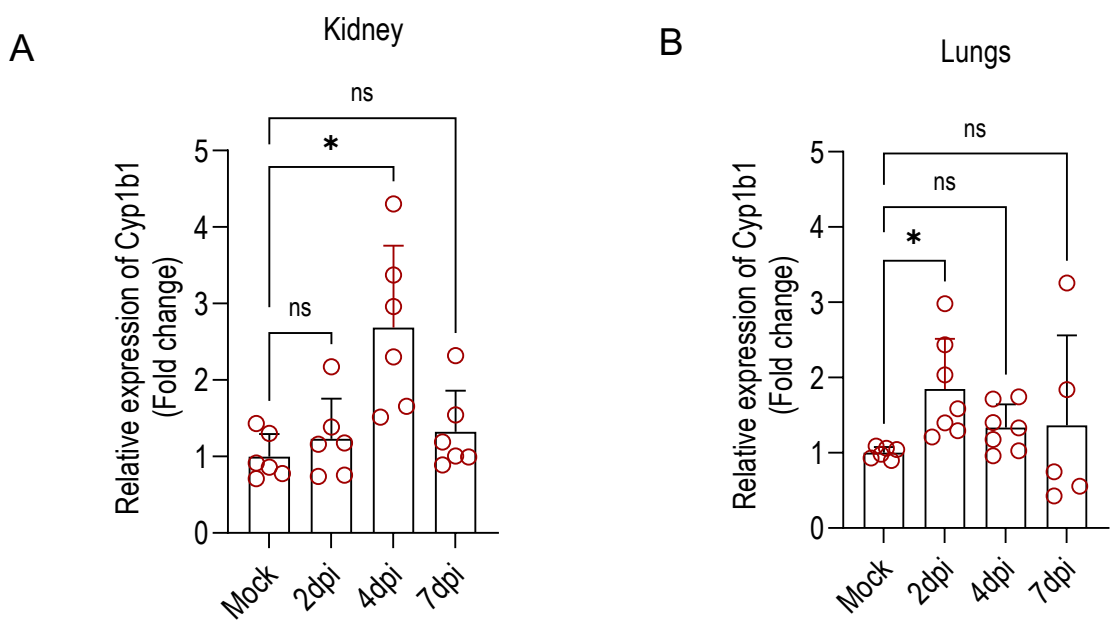

Supplemental Figure 3

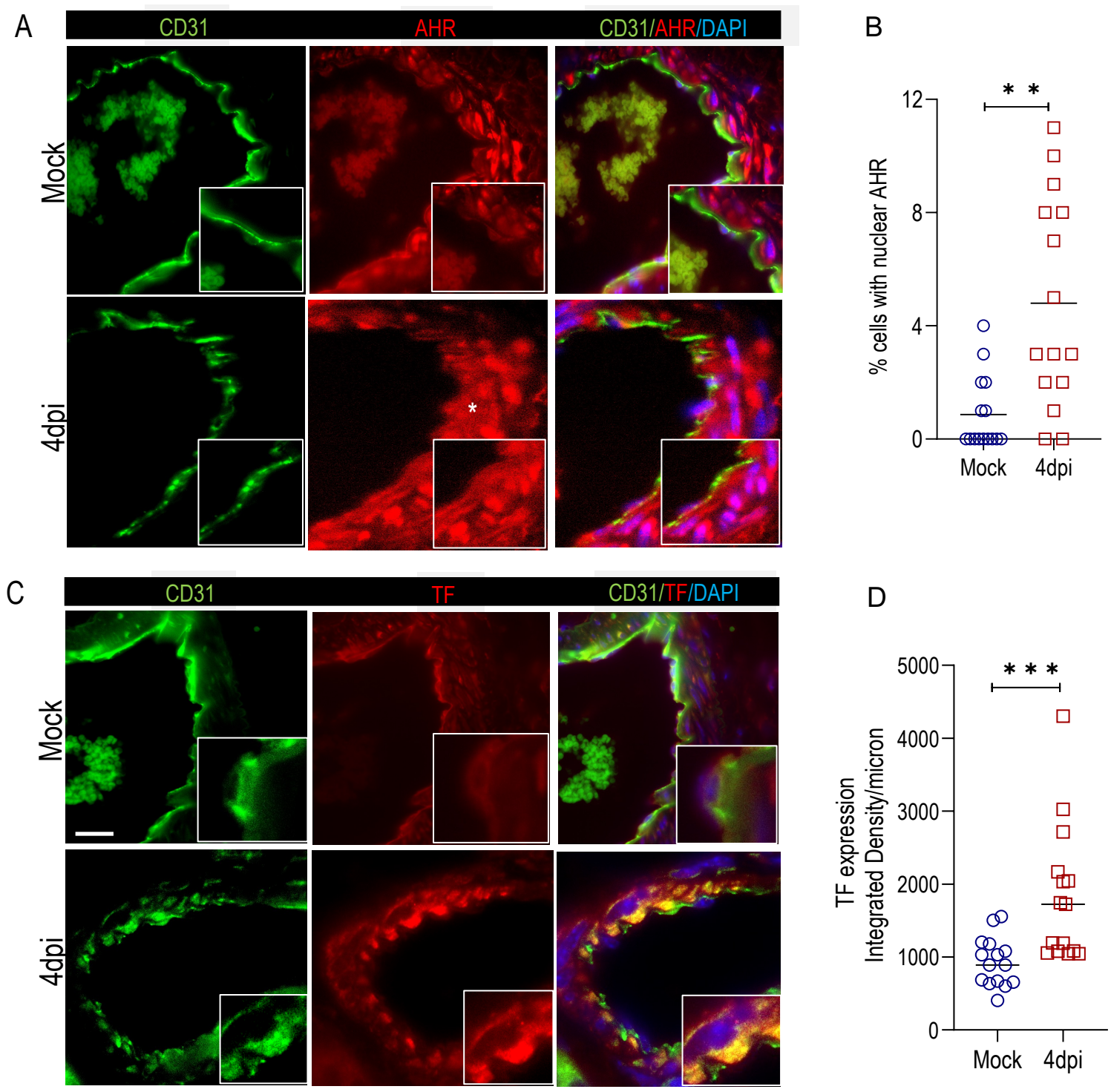
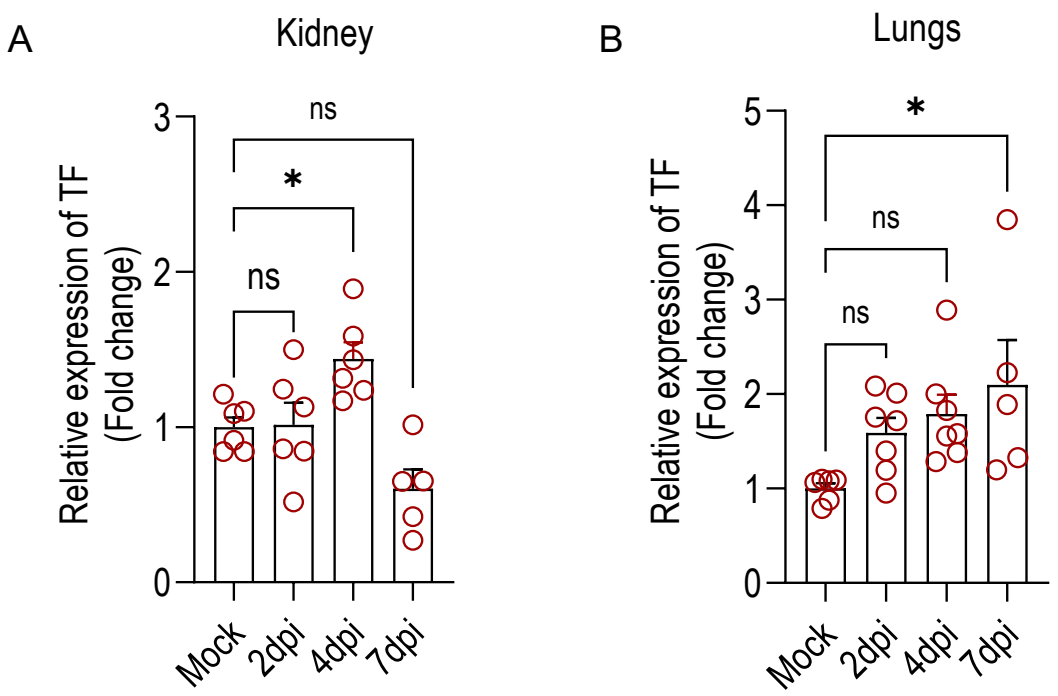
Supplemental Figure 4